



Adapting Passive Microwave-Based Precipitation Algorithms to Variable Microwave Land Surface Emissivity to Improve Precipitation Estimation from the GPM Constellation

F. JOSEPH TURK,^a SARAH E. RINGERUD,^{b,c} YALEI YOU,^{b,d} ANDREA CAMPLANI,^{e,f} DANIELE CASELLA,^f GIULIA PANEGROSSI,^f PAOLO SANÒ,^f ARDESHIR EBTEHAJ,^g CLEMENT GUILLOTEAU,^h NOBUYUKI UTSUMI,ⁱ CATHERINE PRIGENT,^j AND CHRISTA PETERS-LIDARD^c

^aJet Propulsion Laboratory, California Institute of Technology, Pasadena, California

^bEarth Systems Science Interdisciplinary Center, University of Maryland, College Park, College Park, Maryland

^cNASA Goddard Space Flight Center, Greenbelt, Maryland

^dCooperative Institute for Satellite Earth Systems Studies, University of Maryland, College Park, College Park, Maryland

^eSapienza University of Rome, Rome, Italy

^fInstitute of Atmospheric Science and Climate, National Research Council of Italy, Rome, Italy

^gDepartment of Civil, Environmental and Geo-Engineering, University of Minnesota, Twin Cities, Minneapolis, Minnesota

^hDepartment of Civil and Environmental Engineering, University of California, Irvine, Irvine, California

ⁱKyoto University of Advanced Science, Kyoto, Japan

^jLaboratory for Studies of Radiation and Matter in Astrophysics and Atmospheres, l'Observatoire de Paris, Paris, France

(Manuscript received 10 December 2020, in final form 7 April 2021)

ABSTRACT: A fully global satellite-based precipitation estimate that can transition across the changing Earth surface and complex land/water conditions is an important capability for many hydrological applications, and for independent evaluation of the precipitation derived from weather and climate models. This capability is inherently challenging owing to the complexity of the surface geophysical properties upon which the satellite-based instruments view. To date, these satellite observations originate primarily from a variety of wide-swath passive microwave (MW) imagers and sounders. In contrast to open ocean and large water bodies, the surface emissivity contribution to passive MW measurements is much more variable for land surfaces, with varying sensitivities to near-surface precipitation. The NASA–JAXA Global Precipitation Measurement (GPM) spacecraft (2014–present) is equipped with a dual-frequency precipitation radar and a multichannel passive MW imaging radiometer specifically designed for precipitation measurement, covering substantially more land area than its predecessor Tropical Rainfall Measuring Mission (TRMM). The synergy between GPM's instruments has guided a number of new frameworks for passive MW precipitation retrieval algorithms, whereby the information carried by the single narrow-swath precipitation radar is exploited to recover precipitation from a disparate constellation of passive MW imagers and sounders. With over 6 years of increased land surface coverage provided by GPM, new insight has been gained into the nature of the microwave surface emissivity over land and ice/snow-covered surfaces, leading to improvements in a number of physically and semiphysically based precipitation retrieval techniques that adapt to variable Earth surface conditions. In this manuscript, the workings and capabilities of several of these approaches are highlighted.

SIGNIFICANCE STATEMENT: High-resolution satellite-based precipitation data products are currently produced by combining data products from many individual satellites as they orbit Earth. However, the signals recorded by the sensors on board these satellites are not directly related to the precipitation falling near Earth's surface, but rather to a mixture of the precipitation and the underlying Earth surface conditions. The challenge for the algorithms is to be able to effectively separate and extract the desired portion of the signal representing the precipitation, from the undesired portion that is attributed to Earth's surface. A review of a number of methods for carrying out this procedure are described and demonstrated, which capitalize on many years of satellite observations collected over many different Earth surface conditions.

KEYWORDS: Land surface; Precipitation; Snow; Winter/cool season; Algorithms; Microwave observations; Radars/Radar observations; Satellite observations

1. Introduction

For many hydrological, climate, and weather forecasting applications, an important quantity is the amount of precipitation that falls on Earth's surface over a given time interval, i.e., the surface precipitation rate. A fully global satellite-based

Corresponding author: F. Joseph Turk, jturk@jpl.caltech.edu

DOI: 10.1175/JHM-D-20-0296.1

© 2021 American Meteorological Society. For information regarding reuse of this content and general copyright information, consult the [AMS Copyright Policy](#) ([www.ametsoc.org/PUBSReuseLicenses](#)).

Brought to you by University of Maryland, McKeldin Library | Unauthenticated | Downloaded 06/19/24 02:23 PM UTC

precipitation estimate that can transition across changing Earth surface conditions and complex land–water boundaries is an important capability for proper evaluation of the precipitation produced or diagnosed in weather and climate models (Tapiador et al. 2019; Byrne and O’Gorman 2015).

However, no satellite instrument is unambiguously sensitive to the instantaneous precipitation rate at Earth’s surface. Since 1987 with the advent of the operational Special Sensor Microwave Imager (SSM/I), satellite precipitation datasets produced from a variety of scanning passive microwave (MW) radiometers have formed the basic building blocks of nearly all global precipitation datasets (Tapiador et al. 2012; Kidd et al. 2018). These measurements are not *directly* sensitive to the near-surface rain, but rather to Earth’s surface, further modulated by the emission/scattering properties of the intervening water vapor and condensed water structure. In general, the height of the “peak” sensitivity increases as the radiometer channel wavelength decreases, up to infrared (IR) radiometers, which are directly sensitive only to the condensed water at the very top of the cloud (Haddad et al. 2017). Inversion of the passive MW equivalent blackbody brightness temperature (TB) measurements into precipitation estimates (either a single near-surface level, or multiple vertical levels) that perform in a consistent fashion across the variety of complex Earth surface conditions is inherently challenging. In contrast to oceanic surfaces, the radiometers view against a high and variable emissivity surface (~ 0.9 for dry soils) background, providing poor radiometric contrast between the surface and the condensed water structure above the surface. In this manuscript, the term “complex surfaces” refers to land surfaces whose emissivity is controlled by a large number of factors such as vegetation conditions, soil type and moisture (Harrison et al. 2015), and (for frozen surfaces) the snow and/or ice properties (Hirahara et al. 2020), but also surfaces whose geophysical properties are not homogeneous over the resolution of the PMW radiometer field of view including mixed land–water (Gouweleeuw et al. 2012) and coastal boundaries (Mega and Shige 2016). Shortcomings of satellite-based precipitation over these complex surfaces have been highlighted in the reports of the International Precipitation Working Group (IPWG) as far back as the 2004 workshop (Levizzani et al. 2018).

It is not the intent of this manuscript to describe (or estimate) the physical properties that control the microwave surface emissivity (Ferraro et al. 2013). In this manuscript, a review of several promising research methods for precipitation estimation are described that *adapt* to the surface emissivity over complex surfaces, with a focus on the passive MW observations collected by the joint National Aeronautics and Space Administration (NASA) and Japanese Aerospace Exploration Agency (JAXA) Global Precipitation Measurement (GPM) mission (2014–present) (Hou et al. 2014). The GPM core satellite 65° orbit inclination observes substantially more land surface than its predecessor Tropical Rainfall Measuring Mission (TRMM) (Kummerow et al. 1998). (Hereafter, GPM and TRMM are collectively termed the Precipitation Measurement Missions, or PMM). GPM and TRMM are satellite constellation-based measurements, designed around the transfer of information from a narrow-swath precipitation radar (Dual Frequency Precipitation Radar for GPM, Ku/Ka band or 14/35 GHz, denoted by DPR;

and the Precipitation Radar for TRMM, Ku band only, denoted by PR) on the core spacecraft, to the constellation of wide-swath passive MW radiometers, producing a consistent suite of global precipitation products (Skofronick-Jackson et al. 2018). The GPM Microwave Imager (GMI) observations are taken near coincidentally with the DPR on the core satellite, but the other constellation members have passive MW-only capabilities. There are two radar-based precipitation products produced from the GPM core spacecraft, the Combined Radar–Radiometer Algorithm (CORRA) (Greco et al. 2016), and the DPR radar-only algorithm (Seto et al. 2013), both of which have a single-frequency (Ku band), and for GPM, a dual-frequency (Ku/Ka band) variant of their respective precipitation algorithms.

Table 1 lists the current (late 2020) structure of the GPM passive MW constellation. Each passive MW radiometer type is designed with a unique set of channels, each with a unique antenna beamwidth, receiver characteristic, and scan pattern. Together with the orbital properties of the satellite upon which the radiometer is deployed, these parameters determine the Earth incidence angle, channel resolutions, and swath width (Berg et al. 2016). The various constellation satellites observe under different environmental characteristics (e.g., temperature and water vapor structure), and surface physical conditions such as the near-surface skin temperature at the time of the satellite overpass (Tian et al. 2015). Furthermore, the passive MW precipitation estimation algorithm has to accommodate a range of space–time variability in the microwave land surface emissivity. In the common 10–90-GHz regime, the surface emissivity is controlled by key geophysical conditions such as the surface roughness, soil moisture, and vegetation type and water content (Ferraro et al. 2013; Turk et al. 2014a; Tian et al. 2015). These conditions (both surface and environmental) form the background TB from which the presence of precipitation is to be discriminated (Munchak and Skofronick-Jackson 2013). While surface conditions change slowly across seasons, they can also change more rapidly (minutes to weeks) during rapidly changing temperature and weather patterns. Precipitation that reaches the surface in solid phase (snowfall) is especially difficult to contrast from the surface, especially during cold periods when the surface is already snow and/or ice covered (Ebtehaj and Kummerow 2017; Panegrossi et al. 2017; You et al. 2017b). Ideally, the precipitation products produced from the constellation passive MW observations are consistent across varying surface and environmental conditions, so as to introduce minimal artifacts into further gridded Level 3 global products, such as the Integrated Multisatellite Retrievals for GPM (IMERG) (Tan et al. 2019) and other global precipitation datasets (Sun et al. 2017).

Prior to the launch of TRMM, passive MW precipitation retrieval over land surfaces was done using largely empirical methods, typically involving empirical relationships relating 85 GHz (or higher frequency) TB depressions (due to scattering by the high-albedo ice aloft) to surface precipitation inferred from ground radars (Grody 1991; Ferraro et al. 2000). The lower frequencies (<85 GHz) were used for precipitation over ocean and to discriminate particle scattering (originating within the precipitation media) from surface scattering due to snow cover and dry and barren land surfaces. Scattering-based methods perform best for mature convective rain systems

TABLE 1. Center frequencies of the passive MW radiometer channels carried in the GPM Level 1C data available through the PPS, from 2014 to present. Conical-track resolution is given as across track \times along track. Cross-track sensors are indicated with an asterisk, and the resolution and polarization (V/H) is valid only at nadir. LF = Low frequency, HF = high frequency, and LTAN = local time of ascending node. N/A = not applicable.

Satellite	Sensor	LF channels (GHz)	Resolution (km)	HF channels (GHz)	Resolution (km)	Swath (km)	Pixels/scan	LTAN (2020)
Global Precipitation Measurement (GPM)	GPM Microwave Imager (GMI)	10.65 (V/H)	32 \times 19	166.0 (V/H)	6 \times 4	880	221	65-day repeat
		18.65 (V/H)	18 \times 11	183.3 \pm 3 (V)	6 \times 4			
		23.8 (V)	16 \times 10	183.3 \pm 7 (V)	6 \times 4			
Global Change Observation Mission for Water (GCOM-W1)	Advanced Microwave Scanning Radiometer (AMSR-2)	36.5 (V/H)	15 \times 9	—	—			
		89.0 (V/H)	7 \times 4	—	—			
		10.65 (V/H)	42 \times 24	N/A	N/A	1450	243 (LF except 89 GHz), 486 (89 GHz)	1330
		18.65 (V/H)	22 \times 14					
		23.8 (V/H)	19 \times 11					
Defense Meteorological Satellite Platform (DMSP)	Special Sensor Microwave Imager Sounder (SSMIS)	36.5 (V/H)	12 \times 7					
		89.0 (V/H)	5 \times 3					
		19.35 (V/H)	74 \times 45	150 (H)	16 \times 13	1700	90 (LF except 91 GHz), 180 (91 GHz, HF)	1600
		22.235 (V)	74 \times 45	183.3 \pm 1	16 \times 13			1840
		37.1 (V/H)	45 \times 28	183.3 \pm 3	16 \times 13			1720
National Polar-Orbiting Partnership Program (NPP) Joint Polar Satellite System (JPSS-1 or NOAA-20)	Advanced Technology Microwave Sounder (ATMS)*	91.7 (V/H)	16 \times 13	183.3 \pm 6.6 (H)	16 \times 13			
		23.8 (V)	96	165.5 (V)	16	2500	96	1330
		31.4 (V)	96	183.3 \pm 1	16			
		88.2 (V)	32	183.3 \pm 1.8	16			
		—	—	183.3 \pm 3	16			
NOAA-18 NOAA-19 MetOp-A MetOp-B MetOp-C Megha-Tropiques	Microwave Humidity Sounder (MHS)*	—	—	183.3 \pm 4.5	16			
		89.0 (V)	16	157.0 (V)	16	2500	90	2030
		—	—	183.3 \pm 7 (H)	16			1700
		—	—	183.3 \pm 1	16			2100
		—	—	183.3 \pm 3 (H)	16			2130
Sounder for Probing Vertical Profiles of Humidity (SAPHIR)*	—	—	—	191.3 (V)	16			2130
		—	—	183.3 \pm 0.2	10	1700	182	51-day repeat
		—	—	183.3 \pm 1.1	10			
—	—	183.3 \pm 2.8	10					
—	—	183.3 \pm 4.2	10					
—	—	183.3 \pm 6.8	10					
—	—	183.3 \pm 11 (H)	10					

carrying a well-developed ice canopy regardless of surface type, but are less suited for decaying convection (where the upper-level ice has spread out, with stratiform precipitation) or precipitation that evolves with little or no ice phase. Since these algorithms would switch between emission and scattering based methods, from the passive MW imagery it was often unclear whether gradients in precipitation intensity along land–ocean boundaries were physically realistic, or an artifact of the precipitation retrieval method. A scattering index-based method was used for the passive MW overland algorithm for TRMM prior to 2014 (Wang et al. 2009; Gopalan et al. 2010). The current facility algorithm for the PMM missions, the Goddard profiling algorithm (GPROF), is based on Bayesian-based precipitation estimation methods (Tassa et al. 2003; Ringerud et al. 2015). This is due to the abundance of GPM and TRMM radar–radiometer observations available to construct sufficiently representative a priori datasets (Ringerud et al. 2015).

Of interest to this manuscript are PMW precipitation estimation methods that utilize all spectral channels of the constellation PMW radiometers, to adapt to the microwave surface emissivity and environmental conditions. While the poor radiometric contrast has traditionally limited the use of lower-frequency channels (19 GHz and lower) for direct overland precipitation estimation, these same channels exhibit strong polarization differences [TB at vertical (V) polarization > TB at horizontal (H) polarization] over certain surface types (Norouzi et al. 2015). The surface emissivity is highly correlated in the 10–90-GHz range common to many across-track scanning PMW radiometers in Table 1 (Prigent et al. 2006; Bytheway and Kummerow 2010; Turk et al. 2014b), forming the basis for a microwave-based land surface classification (Aires et al. 2011). Furthermore, these correlated properties can be used to constrain PMW methods and improve the detection of snow and light precipitation (Ebtehaj et al. 2020). On some radiometers, the fields of view of the various channels overlap, enabling resolution enhancement (Petty and Bennartz 2017) to distinguish precipitation signatures along coastlines and other strong gradients in surface emissivity.

On the higher end of the spectrum, the >90-GHz channel suite common to operational across-track scanning passive MW sounders (which contribute the bulk of the global GPM coverage) is optimized for the purpose of sensing atmospheric water vapor (Kidd et al. 2018). In this manuscript, observations at frequencies above 95 GHz are termed “high frequency” (HF) observations. The 183.31-GHz channels common to MW sounders are nearly opaque to all Earth surface conditions, the exceptions being regions of very dry air conditions where the total column precipitable water vapor (TPW) < 15 mm, commonly found in arid, dry regions and cold seasons where snow cover is prevalent. For these sensors, a passive MW technique should adapt by providing more weight to the environmental (atmospheric water vapor and temperature profile) conditions at the satellite overpass time (Casella et al. 2015; Skofronick-Jackson and Johnson 2011).

Section 2 provides a brief description regarding how the surface is accommodated in the current (2020) passive MW algorithm (GPROF) for the GPM and TRMM constellation.

Subsequent sections highlight individual methods for improving the estimation of precipitation over complex surfaces:

- **section 3:** implementation of time-changing, dynamic surface properties (Ringerud et al. 2020);
- **section 4:** temporal change detection between passive MW satellite revisits (You et al. 2018);
- **section 5:** surface emissivity structure for a priori data indexing (Turk et al. 2017);
- **section 6:** TB-based supervised machine learning for precipitation detection (Takbiri et al. 2019);
- **section 7:** frozen surface spectral signature signal for snowfall retrieval (Camplani et al. 2021);
- **section 8:** spatial information in TB patterns to separate the surface and precipitation (Guiloteau and Foufoula-Georgiou 2020).

The manuscript concludes with future directions that are in their early stage of development, such as machine-learning methods, and indirect methods (e.g., soil moisture–deduced inference of time-accumulated precipitation). We note that orographically enhanced precipitation, while a surface-related process, is not examined in this study, since it is more related to the motion and direction of the lower-/midtropospheric water vapor above the surface (Yamamoto et al. 2017). Furthermore, over-ocean precipitation estimation is not specifically addressed. The factors that control the emissivity of open water bodies are generally well modeled (Meissner and Wentz 2012), although it is recognized that uncertainty exists under low sea surface temperatures or high wind speeds (Kilic et al. 2019). Finally, it is noted that this is not intended as an exhaustive review; there may be similarly related research or methods that the authors have overlooked or are unaware of.

2. Background of the surface emissivity scheme used in GPROF

The current GPM facility algorithm for constellation passive MW processing (GPROF) (Kummerow et al. 2015) is designed around a Bayesian method to locate and weight a priori observations most congruent to the input TB observation. The a priori data use precipitation profile retrievals produced by the CORRA algorithm to forward model the TB for each sensor in Table 1 (Ringerud et al. 2019). In practice, adjustments are done to the a priori dataset to account for the nature of the marginal probability (precipitation rates are not equally distributed; some conditions occur very infrequently), and limitations of the radar data used to build the a priori. For example, the DPR and PR radars are fairly insensitive to non-precipitating clouds (Kubota et al. 2020), light rain (<0.5 mm h⁻¹) (Hamada and Takayabu 2016), cloud ice (Ringerud et al. 2019), and light snowfall (Skofronick-Jackson et al. 2019). The GPROF a priori dataset is augmented with auxiliary sources to properly account for these conditions while retaining radiometric consistency. This includes replacement of the CORRA precipitation profiles with data from surface radar over snow covered surfaces (NASA 2017).

To reduce the search for prior observations under similar surface conditions, the overland algorithm is constrained

TABLE 2. Value of the surface classification index used in GPROF.

Surface class index	Description	Properties
1	Ocean or large inland water body	—
2	Sea ice	—
3–7	Decreasing vegetation cover	3 = Amazon, 7 = Sahara Desert
8–11	Decreasing snow cover	(8 = Antarctica, 11 = lightly snow covered). Overwritten by daily land snow = 10.
12	Inland water, rivers, estuaries	—
13	Coastline, land/water boundary	—
14	Ocean/sea ice boundary	—

using a surface classification index derived from a monthly emissivity climatology (Aires et al. 2011; Prigent et al. 2006). The surface classification is uncoupled from (not related to, or dependent upon) the coincident atmospheric environmental conditions. The values of the current surface classification index are provided in Table 2. For example, a pixel location with surface class value of 4 (moderate vegetation) does not change whether the surface temperature is unseasonably low or high, or has experienced high antecedent precipitation conditions; it will always look for surface class 4 when performing its search of a priori data. However, it is recognized that the use of a climatological classification is not applicable at the per-pixel level snow or ice cover. A climatology can express the probability of snow or ice cover on given date, but the actual snow or ice cover on the surface (at the satellite overpass time) is a result of recent weather events and temperature conditions. Therefore, the current incarnation (version 5) of GPROF uses the daily Global Multisensor Automated Snow/Ice Mapping System (commonly referred to as Autosnow) product (Romanov et al. 2000) to overwrite the surface classification index whenever Autosnow indicates snow cover. This index provides a convenient way to accommodate the actual snow or ice surface emissivity to first order, but it does not accommodate the complex snow or ice morphology, which is further addressed in section 7. Vegetation and soil moisture properties, two characteristics that are known to modulate the microwave surface emissivity (Turk et al. 2014a; Ringerud et al. 2020) are reduced to the five vegetation classes. It is recognized that a climatological surface classification method is not designed to adapt to surface emissivity change on scales ranging from subhourly (e.g., soil moisture change following the onset of precipitation) to days (e.g., appearance/disappearance of transient water bodies, ice–snow transitions). These emissivity changes are what drive the rationale for the material shown in sections 4 and 5 below.

GPROF further constrains its search of the a priori dataset with the 2-m air temperature (T2m) and TPW conditions, interpolated from (for near-real-time products) an operational global weather forecast model (later reprocessing of the GPROF data utilize these same quantities interpolated from the ERA model reanalysis). These three terms (surface classification index, T2m and TPW) are used to stratify the large a priori dataset for each passive MW radiometer in the constellation. Since these three terms can also be obtained at any subsequent satellite overpass time; they provide the link into

the a priori database to identify TB that are most congruent to the observed TB. Further details are provided in Kummerow et al. (2015) and in the GPROF Algorithm Theoretical Basis Document (ATBD) (NASA 2017).

As stated, a main intent of this manuscript is to examine other means to advance the land surface constraint beyond a fixed climatological classification. Below, the precipitation estimation methods that address the underlying surface conditions (end of section 1) are described.

3. Dynamic surface properties/emissivity methods

Recent advances to PMW precipitation retrieval over land have been achieved through the use physically based methods. Physically based methods require some estimate of the instantaneous emissivity so that the precipitation signal can be separated from the background emission. This is more difficult over land due to the dynamic nature of the emissivity as well as its large signal in comparison to that identifying the precipitation. In heavy precipitation cases, the retrieval is insensitive to the surface; however, for light precipitation cases the emissivity becomes highly relevant in any physically based retrieval developed for land surfaces.

Physical models of emissivity, such as those included in the NOAA Community Radiative Transfer Model (CRTM) (Liu and Boukabara 2014) and the Community Microwave Emission Modeling Platform (CMEM) implemented by the European Centre for Medium-Range Weather Forecasts (ECMWF) models (de Rosnay et al. 2020), require detailed information about the instantaneous surface state above and below the surface, as well as a radiative transfer model to compute the radiance of each layer and interface. The methods are often optimized for frequencies < 20 GHz. Comparisons between modeled emissivities and satellite-derived ones have been performed (Prigent et al. 2015) and, especially over snow-covered areas (Yan et al. 2008), the models perform poorly; the interaction between the medium and the radiation is complex and the input parameters to the model are not available (e.g., snow depth, snow wetness, particle sizes). These modeled values can be used to compute dynamic (real-time) emissivity values for use in constraining the algorithm, as well as the forward TB modeling necessary for creation of the constellation GPROF radiometer databases for the GPM constellation (Kummerow et al. 2015). Ringerud et al. (2014) developed a semiempirical model for microwave emissivity using modeling

concepts from both CRTM and CMEM along with land surface model inputs over the U.S. Southern Great Plains area. This model was implemented in a test bed database for precipitation retrieval (Ringerud et al. 2015), demonstrating modest improvements over climatological emissivities in simulation of TB values over land for GPROF constellation retrievals. The drawback to such methods is the need for instantaneous information about the surface state including vegetation, soil type, soil moisture, and even the presence of dew, for emissivity model input on a global scale.

An additional approach is to constrain the retrieval using retrieved surface emissivity values. Microwave emissivity retrieval has a long history (Prigent et al. 2006; Wang et al. 2017), and recent work deriving a retrieval for GPM shows the utility of such retrievals (Munchak et al. 2020). A method for integrating this information into a passive MW precipitation retrieval using a hybrid optimal estimation (OE)–Bayesian technique is presented in Ringerud et al. (2020); an example of implementation of the technique for the GPM GMI is described here.

The first step in the hybrid retrieval process is an OE-based nonraining retrieval. This retrieval is described in detail in Munchak et al. (2020) and includes as output surface emissivity at each radiometer frequency, TPW, and an error parameter describing how well the algorithm converges under the assumption of a hydrometeor-free atmosphere. This error parameter can then be used to detect areas of precipitation, as the nonraining retrieval will not be able to converge in the presence of precipitation.

The emissivity retrieved in the first step can be used to determine the presence of snow cover, which is important in passive microwave precipitation retrieval, as snow cover can be mistaken for a precipitation signal (Yan et al. 2008). A demonstration of this is pictured in Fig. 1 for a GMI overpass on 6 December 2015. The snow cover identification scheme compares retrieved emissivity values at the GMI 18.7- and 89.0-GHz V-pol channels to monthly mean snow-free emissivity values for each location. Snow cover is detected when there is a combination of an emission (increased emissivity) signal as compared to the snow-free mean in the lower frequency, and a scattering (decreased emissivity) signal in the higher frequency. Figure 1 shows retrieved emissivity at these two channels in the top panels, with the detection scheme results in the lower right. The NOAA Autosnow product for this day is shown in the lower-left panel for reference. The Autosnow product is currently used operationally for GPROF retrievals, and has some drawbacks including that it is a daily product, whereas using the instantaneous emissivity has the benefit of accounting for new snow and melting throughout the day.

Next the error parameter, describing how well the OE algorithm converges under the assumption of a hydrometeor-free atmosphere, output by the nonraining retrieval is used to determine areas of possible precipitation. Ringerud et al. (2020) test varying thresholds globally. Figure 2 shows an example GMI overpass from 4 June 2016, using error parameters ranging from 0 to 0.5. Where the error parameter exceeds the cutoff value, a Bayesian retrieval similar to GPROF is

performed. Rather than use the climatological surface classification and forecast model information to constrain the retrieval, however, the emissivity at 18.7 GHz and retrieved TPW are used. The 18.7-GHz channel is chosen as similar frequencies exist on all GPM constellation imagers. A drawback to this approach is that emissivity and TPW cannot be accurately retrieved in the presence of heavy precipitation. In the retrieval, any retrieved values with error parameter above a threshold indicating even light precipitation is discarded. Retrieved values from the surrounding footprints are interpolated across such areas and the constraints on the Bayesian database are relaxed to allow for the possibility of higher values in precipitating areas. For the emissivity constraint, the recent seasonal mean value retrieved from prior precipitation-free overpasses is used, and the constraint is relaxed to allow for precipitation effects on the surface (i.e., an area of the database is searched ranging from the interpolated value over a small interval of decreased emissivity and increased TPW as would be expected in precipitating conditions). A cutoff value of zero indicates no previous knowledge of precipitating areas, and the Bayesian is used everywhere, and as values increase the Bayesian is run only in areas where the nonraining retrieval has more and more trouble finding a solution. This is well illustrated in the example of Fig. 2 [see Fig. 3 for the Multi-Radar Multi-Sensor System (MRMS) ground validation data for this case], showing that the area of precipitation decreases as the error parameter cutoff value increases.

While knowledge of the emissivity is shown here to have a potentially large effect on light precipitation retrievals, such methods do not tend to show improvement in persistent underestimation of higher rain rates over land where the contribution of the upwelling TB from the surface becomes irrelevant. It has been demonstrated that adding information to the retrieval about the atmospheric boundary layer state, such as convective available potential energy (CAPE) can improve estimates at these higher rain rates (Casella et al. 2013; Smith et al. 2013; Petković et al. 2017). The ideal solution in a physically based retrieval such as the operational GPM GPROF then, would utilize constraints with sensitivity to both the surface emissivity for improvement of light precipitation estimates, and also information about the dynamic characteristics of the precipitation and associated TB scattering signatures relevant to the retrieval.

Current efforts in this area have a focus on soil moisture as a main component of emissivity, and its indirect connection to atmospheric state as evidenced by the connection between soil moisture and convective initiation (Ford et al. 2018). A GPM-based exploration of the relationship between soil moisture and convective precipitation obtained globally using a land surface model shows a promising link to the observed GMI scattering signal as a function of DPR rain rate (Fig. 4). These connections will be tested as algorithm improvements in future research.

4. Temporal revisit methods

Over much of the land area observed by GPM, the climatological microwave land surface emissivity is near 0.9 and

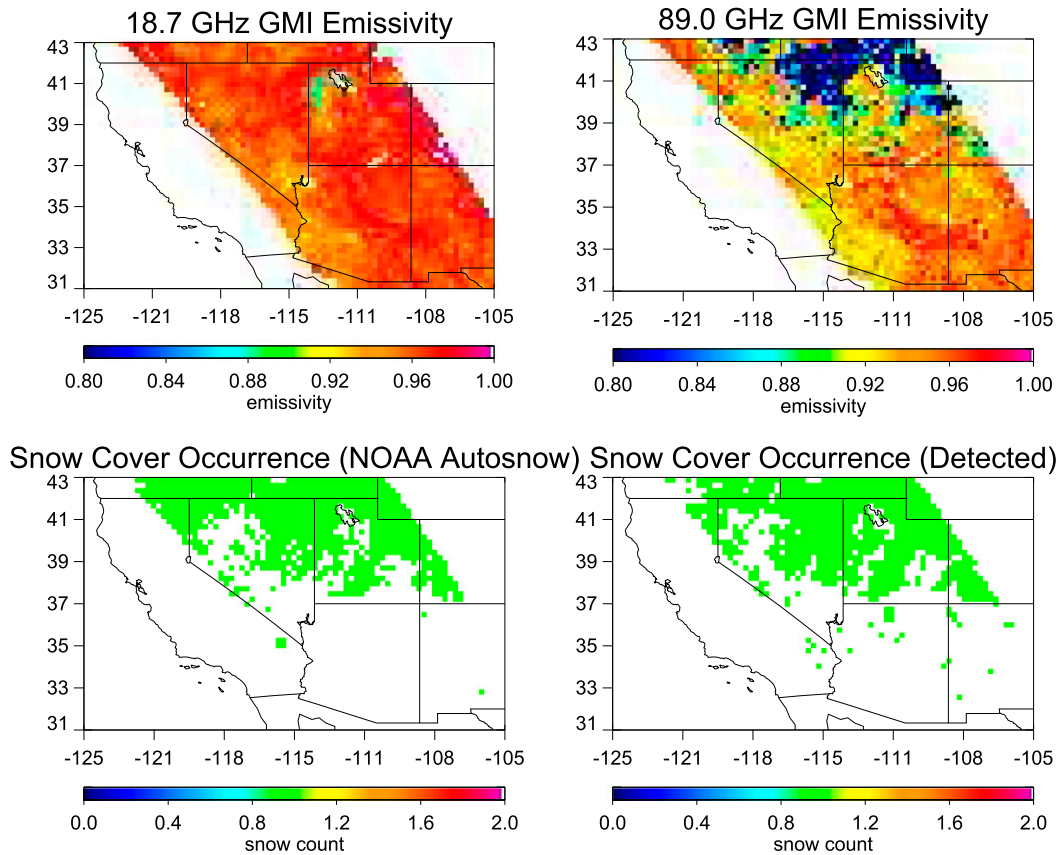


FIG. 1. Snow cover detection example from a GMI overpass on 6 Dec 2015. Emissivity retrievals from the (top left) 18.7-GHz V pol and (top right) 89.0-GHz V pol are used in the detection scheme. (bottom right) Results are shown, with (bottom left) the NOAA Autosnow product included for comparison.

highly heterogeneous (Prigent et al. 2006; Ferraro et al. 2013). Therefore, deviations from this value are difficult to model accurately, especially for HF channels and over snow- and ice-covered regions. The fundamental idea of using the TB temporal variation (referred to as delta-TB, denoted by ΔTB) as a basis for the precipitation retrieval is to capitalize upon the revisit sequence of satellite overpasses from the GPM satellite constellation, to minimize the influence of the surface emissivity. In essence, the ΔTB concept adds the time dimension into the retrieval process to alleviate the surface contribution to the net upwelling TB.

a. Derivation of ΔTB

To derive ΔTB , PMW radiometer observations from 10 polar-orbiting satellites are used, listed in Table 1. The Level 1C intercalibrated TB for the HF channels are used from each sensor (Berg et al. 2016). The Level 1C TB for all satellites are available from March 2014 (launch of the GPM satellite) to December 2019, except periods of missing SSMIS-F16, MHS-NOAA-18, and ATMS-NOAA-20. For SSMIS-F16, the 183-GHz channels were not processed from December 2013 to August 2015 due to quality issues. MHS-NOAA-18 ceased to work in late October 2018. ATMS-NOAA-20 data became available from late November 2017.

In addition, the 150-GHz channel of SSMIS-F18 stopped functioning in February 2012.

You et al. (2017a, 2018) have documented how to implement the ΔTB concept into the precipitation retrieval process. Here, the procedure is briefly summarized.

The TB from the non-GMI satellites is first converted into “equivalent” GMI channels through the simultaneous conical overpass (SCO) technique and a principal component analysis (PCA) (Cao et al. 2004). In contrast to You et al. (2018), the conversion coefficients are derived in each 2.5° grid box instead of over the continental scale. The net result is to transform each non-GMI sensor as if there are 10 sensors measuring at four GMI frequencies, which are 89.0 (V/H) 166.0 (V/H), 183.3 ± 3 (V), and 183.3 ± 7 (V). For convenience, these frequencies are referred to as V89, H89, V166, H166, V186, and V190.

Next, the ΔTB is computed at 89.0 (V/H) 166.0 (V/H), 183.3 ± 3 (V), and 183.3 ± 7 (V) GHz. Similar to the TB naming convention, these ΔTB are referred to as $\Delta V89$, $\Delta H89$, $\Delta V166$, $\Delta H166$, $\Delta V186$, and $\Delta V190$ for convenience. The ΔTB is computed as the current TB associated with precipitation (judged by the linear discriminant analysis method; Turk et al. 2014b; You et al. 2017a) and the preceding TB at the same location without precipitation. In essence, the ΔTB concept is

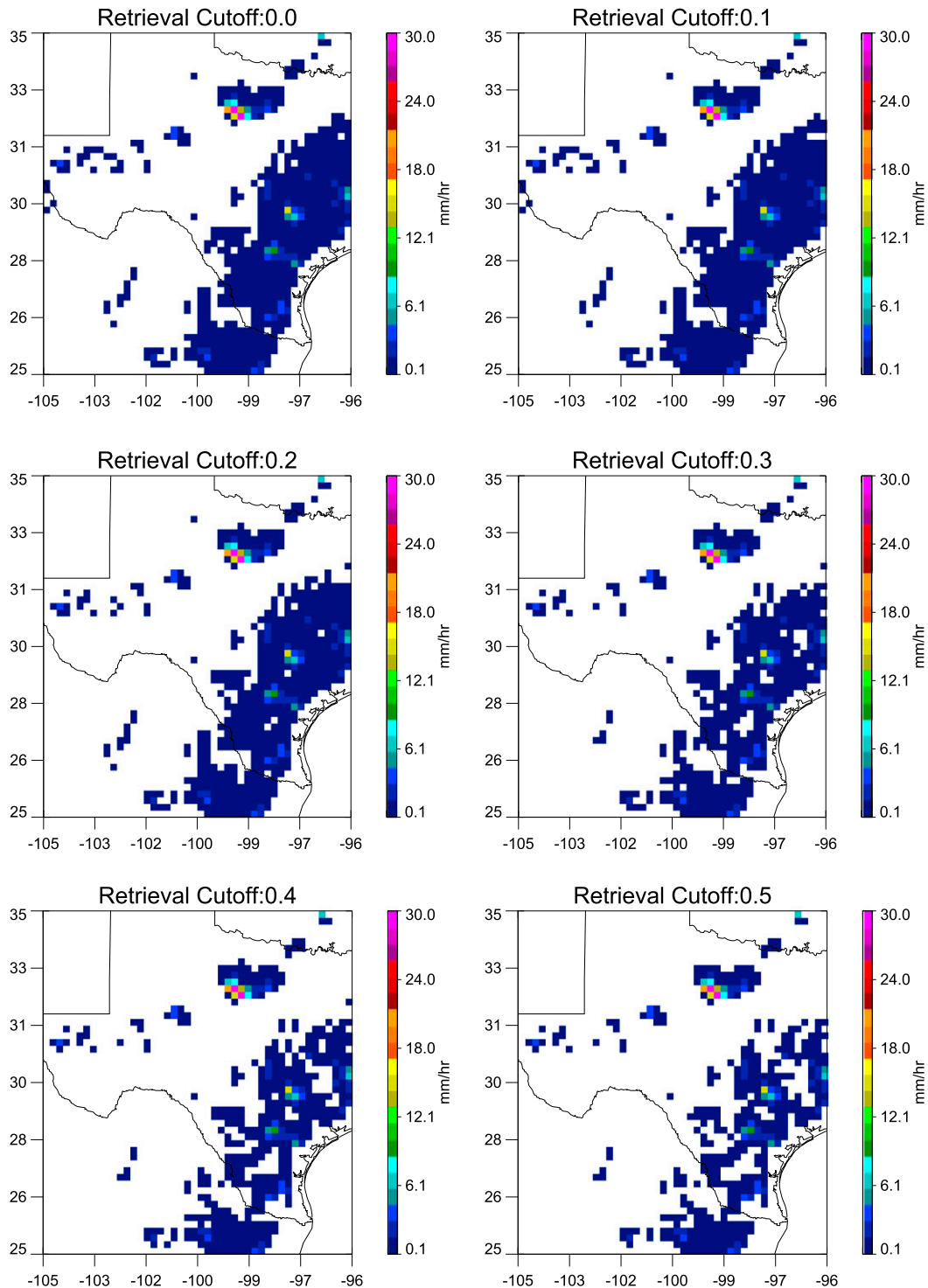


FIG. 2. Demonstration of rainfall retrieved using the hybrid method for cutoff error parameters ranging from (top left) 0 to (bottom right) 0.5 for a GMI overpass on 4 Jun 2016.

to extract the precipitation signal by minimizing the background information, assuming that the surface emissivity and the environmental parameters (e.g., temperature) do not

change rapidly over this time. In the example below, the revisit time from these 10 satellites is on average about 1 h over the Alaska region.

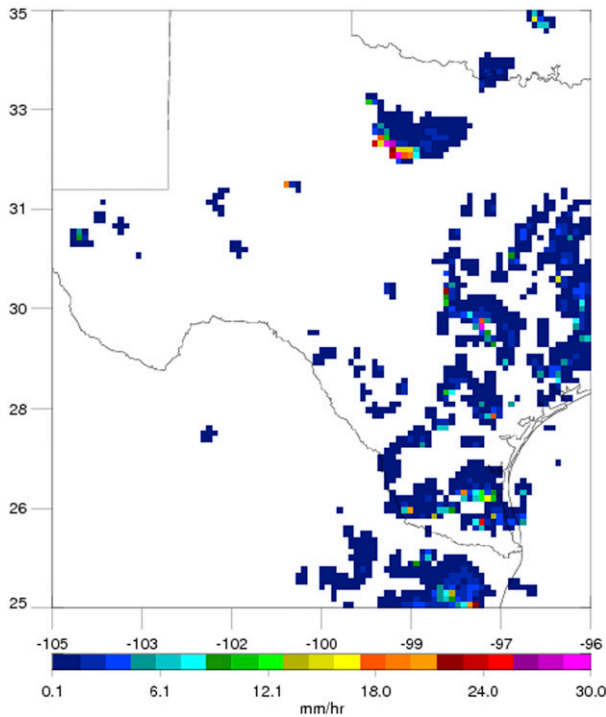


FIG. 3. MRMS surface radar precipitation for the 4 Jun 2016 case shown in Fig. 2.

To compare the retrieval capability between TB and Δ TB, a multiple linear regression model is trained in each 0.25° grid box between the DPR Ku-only precipitation rates and TB observations at V89, H89, . . . , and V190, and between the DPR Ku-only precipitation rates and Δ TB observations at Δ V89, Δ H89, . . . , and Δ V190, respectively. A random selection of 80% of the data are used as the training datasets, and the remaining 20% are used for validation purposes. While simple

linear regression is used as a proof of concept, more advanced statistical approaches (e.g., neural networks and Bayesian methods) may further improve the retrieval performance. Additionally, the retrieval results are compared to the scattering index (SI) approach discussed in section 1 above. There are various forms of the SI definition; this study computes the SI as the TB difference between V89 and V19 (i.e., $SI = V89 - V19$) (Seto et al. 2005). Similarly, the relation between the DPR Ku-only precipitation rates and SI in each 0.25° grid box is established through the simple linear regression approach, and the same ratio (80% and 20% of the data as the training and validation datasets, respectively) is used.

b. Example over Alaska

The Δ TB method for precipitation estimate is evaluated over the Alaska region (land portion of the domain 130° – 170° W, 50° – 65° N), relative to the GPM DPR Ku-only precipitation observations. Figure 5 shows the correlation between DPR Ku-only precipitation rates and TB at V89, V166, and V190, and their Δ TB counterparts of Δ V89, Δ V166, and Δ V190. V89 has a very weak correlation with precipitation. Specifically, the vast majority of the correlation coefficient is weaker than -0.3 over the Alaska regions because of the relatively weak ice scattering from the light precipitation (Fig. 5a). In contrast, the correlation from Δ V89 is greatly improved to -0.7 over the majority of the region (Fig. 5b).

To illustrate this point, Fig. 6a shows the scatterplots between V89 and the DPR Ku-only precipitation rates at the specific 0.25° grid box located at (149.75° – 150° W, 62.5° – 62.75° N). At this location, about 90% of the precipitation rates are less than 1 mm h^{-1} (using DPR from 2014 to 2019). As shown by previous studies (Skofronick-Jackson and Johnson 2011; You et al. 2017a), the 89-GHz TB is still affected by the surface contribution under this light precipitation scenario. In other words, the cold TB (less than 250 K in Fig. 6a) are caused by the low surface emissivity and the low surface temperature,

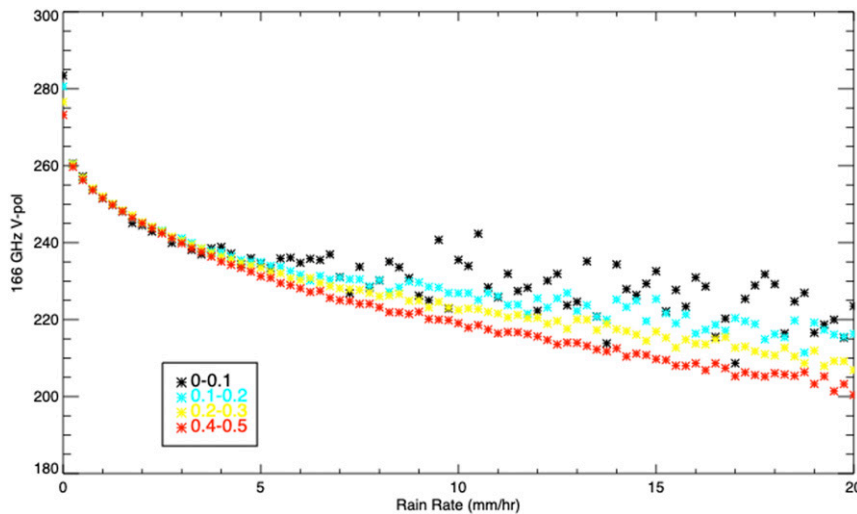


FIG. 4. GMI Tb at 166-GHz V pol as a function of DPR rain rate and soil moisture (colors; $\text{m}^3 \text{ m}^{-3}$) from 1 Sep 2014 through 31 Aug 2015 over all nonfrozen land surfaces.

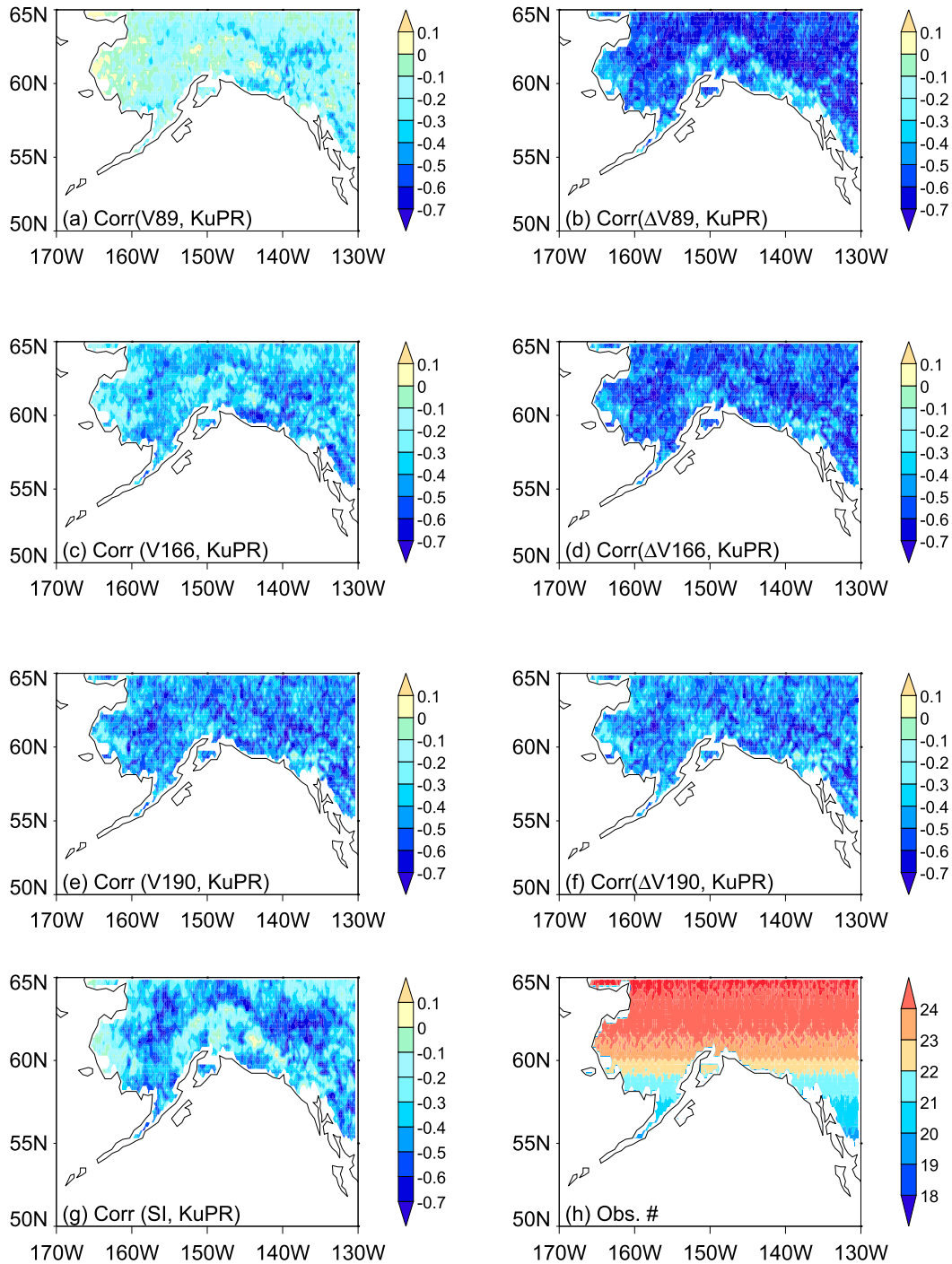


FIG. 5. Correlation maps at each 0.25° grid box. Panels are arranged from left to right beginning in the upper left. Correlation between DPR Ku-only precipitation rates and (a) brightness temperature (TB) at V89 and (b) Δ TB at V89, (c) TB at V166 and (d) Δ TB at V166, and (e) TB at V190 and (f) Δ TB at V190. (g) Correlation between DPR Ku-only precipitation rates and scattering index ($\text{SI} = V89 - V19$), and (h) average daily observation count from the 10 satellites. All data are from March 2014 to December 2019, excluding SSMIS-*FI6*, MHS-*NOAA-18*, and ATMS-*NOAA-20*.

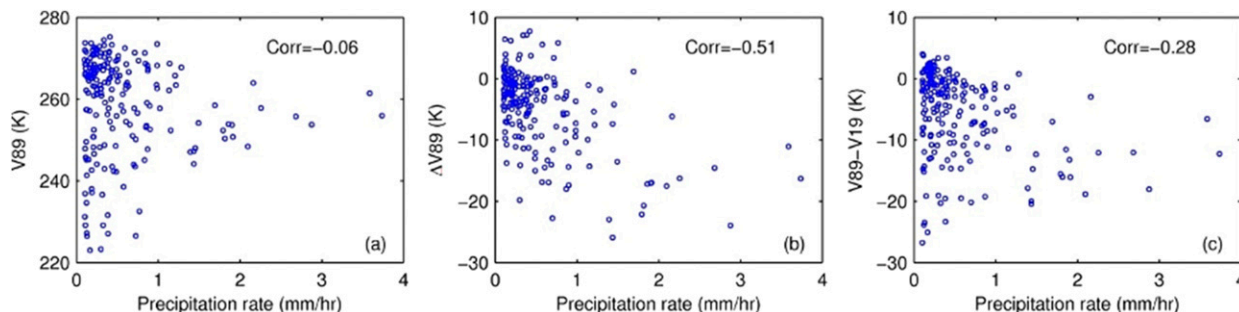


FIG. 6. (a) Scatterplot between DPR Ku-only precipitation rates and V89 at the 0.25° grid box (149.75° – 150° W, 62.5° – 62.75° N), from March 2014 to December 2019. (b) As in (a), but for $\Delta V89$. (c) As in (a), but for scattering index ($SI = V89 - V19$).

instead of by hydrometeor scattering processes. Using the TB temporal variation derived from the 10 satellites, the correlation between the precipitation rate and $\Delta V89$ is improved to -0.51 (Fig. 6b), compared with the correlation being -0.06 from V89 itself. On average, there are about 24 observations each day from these 10 satellites at this location (Fig. 5h), which ensures that the nonprecipitating background is usually available within 1 h. Further, the relation between SI and DPR Ku-only precipitation rates is also analyzed (Fig. 6c). Using the simultaneous V19 as the background, the SI approach can mitigate the surface influence to a certain extent. However, the result from the SI (Fig. 6c) method is not as good as that from $\Delta V89$ (Fig. 6b). This same result is noted in the map panels in Figs. 5b and 5g.

Large improvements have also been noticed by comparing the correlation from V166 and $\Delta V166$ (cf. Figs. 5c and 5d). The improvement from $\Delta V190$ is marginal compared with V190 itself (cf. Figs. 5e and 5f) due to the weak surface influence on V190 channel. The improvement magnitudes from H89, H166, and V186 are similar to those from V89, V166, and V190, respectively.

Figure 7 shows the precipitation retrieval results from (left to right) ΔTB , TB, and SI using the simple linear regression method. As expected, the retrieval performance from ΔTB is better than that from TB, in terms of all three statistical metrics [correlation, root-mean-square error (RMSE), and bias]. The improvement is particularly evident for the light precipitation ($< 2 \text{ mm h}^{-1}$), where the surface contamination is more severe. The results based on the SI approach (Fig. 7c) are noticeably worse than that from TB (Fig. 7b). This may be due to that fact that SI uses information from 19 to 89 GHz, while all frequency channels between 89 and 190 GHz are utilized in the TB retrieval procedure.

5. Separating the a priori data by microwave surface emissivity

The use of principal component (PC) methods for brightness temperature (TB) channel reduction has a long heritage in passive MW precipitation estimation (Petty 2013), typically used in such a way as to “separate” or isolate the desired precipitation signal from the undesired surface emission/scattering signal. The emissivity principal components (EPC) methodology is

designed the other way around, using the more frequent satellite observations gathered under nonprecipitating conditions, to quantify the variability in the microwave surface emissivity, regardless of the surface type (Turk et al. 2017). Increasing deviations from this quiescent, nonraining state form a natural discrimination for the presence of precipitation-affected TB scenes. As the discrimination from the nonraining state becomes more certain, the retrieval candidate selection considers an increasingly larger number of precipitating scenes. Similar to GPROF, the EPC is a precipitation profiling, Bayesian-based inversion technique. It is focused on providing an estimate of the precipitation structure (vertical profile) jointly with the near-surface precipitation rate (Utsumi et al. 2020). A step-by-step process of how the EPC operates is provided in appendix A of Turk et al. (2017) and briefly summarized here.

Essentially, the EPC a posteriori precipitation estimate is designed to transfer the information in the limited swath DPR, to the wider swath of each passive MW radiometer in the GPM constellation, designed around observational a priori databases (DB) built from orbital coincidences with GPM. For GMI, the DPR Ku-band swath covers about the middle one-third of the GMI swath. For the non-GMI radiometers, the a priori DB are created from the collection of all ± 15 -min coincidences between GPM–DPR and each of the constellation radiometers. Each DB entry carries the precipitation profile from the DPR and CORRA algorithms (Greco et al. 2016), averaged to (for conical instruments in Table 1) the resolution of the 37-GHz channel, and (for across-track instruments) the varying pixel resolution in the across-track direction.

Under nonprecipitating conditions, each channel in the observed TB is influenced by differing contributions by the corresponding surface emissivity, the surface skin temperature, and the intervening atmospheric temperature–moisture structure, quantities which are naturally correlated. Similar to Boukabara et al. (2011), for each radiometer a principal component (PC) analysis is carried out on the surface emissivity for all channels near and below 90 GHz, augmented with the surface temperature (T_s), T2m, and TPW from the MERRA-2 reanalysis (Gelaro et al. 2017). While these quantities are not known at the satellite observation time, Turk et al. (2017) showed that the EPC vector can be estimated by nonlinear combinations of the observed TB. The EPC is essentially a

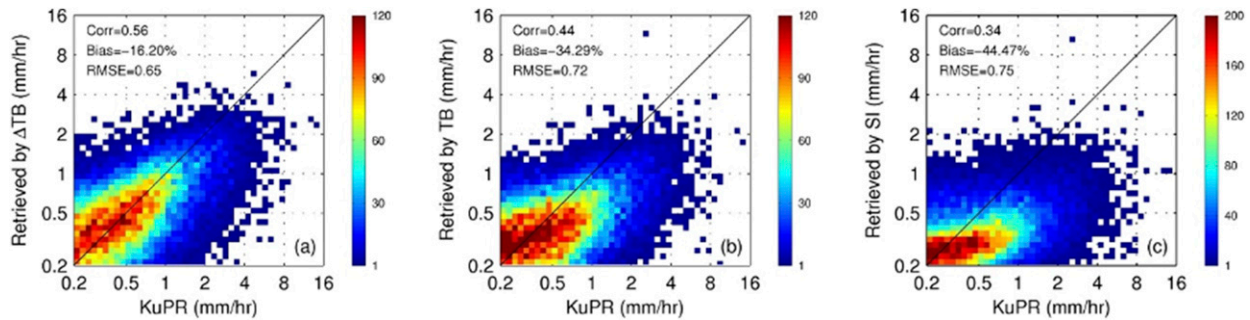


FIG. 7. (a) Precipitation retrieval performance using Δ TB method, (b) precipitation retrieval performance using the TB method, and (c) precipitation retrieval performance using the scattering index ($SI = V_{89} - V_{19}$) method. Correlation, RMSE, and bias are provided for each method.

transformation of the observed TB, computed “on the fly” (and by definition, the emissivity vector can be reconstructed from the EPC vector). The same TB-to-EPC transformation is used to store the EPC values for each entry in the a priori DB. Whereas in the GPROF the a priori databases are clustered separately by a monthly class index, T2m, and TPW, the EPC databases are clustered into N bins that extend across the expected range of each of the first three EPC values. Currently, $N = 29$ bins are used, which discretizes the a priori dataset into $29^3 - 1 = 24\,389$ files (Utsumi et al. 2020). For example, if the first three EPC values fall into bins 10, 8, and 25, the database index is given by $10 \times 29^2 + 8 \times 29 + 25 = 8667$. This is convenient whenever a TB pixel falls into a portion of the a priori database that is sparsely populated, and the search has to expand around this area. In this example, the search expands by gradually incrementing about index 8667 (8666, 8668, 8665, 8669, etc.) until the desired number of a priori candidates are located. Expanding about the lower-order EPC first slowly varies the surface emissivity state. Rather than comparing passive MW observations and a priori candidates by their Euclidean distance in TB space, the comparison is done by distance in EPC space. Since the EPC structure adapts to the joint variability in the surface emissivity and the environmental conditions in the observed TB scene, it removes the need for surface classification and reduces the dependence upon ancillary moisture and temperature state variables.

a. Accounting for the quantities that control the surface emissivity

In Fig. 8, the T2m, TPW, and 37H-GHz emissivity (e_{37H}) are shown for a 5-yr average in Northern Hemisphere summer (July) and winter (January) seasons, computed directly from the GMI TB. The TB is used to estimate the EPC, then the emissivity, T2m, TPW, and T_s are reconstructed from the EPC. Global patterns are well represented and the TB-estimated values exhibit a high degree of correlation (>0.95) with the corresponding MERRA-2 data, with the exception of a $\sim 20\%$ underestimate in TPW across the heavily vegetated South American regions (not shown). In general, the first emissivity PC (EPC1) is smallest over cold, dry, and snow-covered surfaces, and largest over warmer surfaces, whereas the second emissivity PC (EPC2) corresponds with the overall pattern of

TPW, including surface emissivity patterns when $TPW < 15$ mm (not shown). Earlier work by Turk et al. (2014a) applied a physical emissivity model to 8 years (2004–12) to TRMM and WindSat data. Those findings showed a strong correspondence between the first two EPC and the corresponding soil moisture (SM) and vegetation water content (VWC) conditions (cf. Fig. 1 in Turk et al. 2014a).

Figure 9 shows the global map of locations of all entries from one subset (database index 18572) of the EPC-indexed a priori dataset. Expressing in powers of 29, $18572 = 22 \times 29^2 + 2 \times 29^1 + 12 \times 29^0$. Therefore, this database represents candidates with high EPC1 (bin 22), low EPC2 (bin 2), and moderate EPC3 (bin 12). The colors indicate the 3-month interval described in the caption. These entries occur predominantly in very dry, low vegetation conditions in the summer season of each hemisphere. Using the same color scheme to represent the 3-month interval, the top panel of Fig. 10 shows the histogram of the TELSEM index for this same database subset, consisting of very low vegetation conditions (index 7) from Table 2, in accord with the vegetation conditions expected at the locations in Fig. 9.

The bottom four panels in Fig. 10 separate the data from Fig. 9 by their 3-month period, and match the time (nearest day) and location (within 10 km) of each subset entry to the WindSat physical model database. This matchup is done for each year from 2004 to 2012, to gather variability in the physical conditions across the 8-yr period. The majority of the data from June to August (third panel from left) occur where $SM < 0.2$ and $VWC < 5$.

By contrast, Figs. 11 and 12 are identical to Figs. 9 and 10, representing database subset 19146. Expressing in powers of 29, $19146 = 22 \times 29^2 + 2 \times 29^1 + 6 \times 29^0$. Therefore, this database represents candidates with high EPC1 (bin 22), high EPC2 (bin 22), and low EPC3 (bin 6). Figure 11 shows that these database subset entries occur for known areas of high vegetation, in accord with the clustering near TELSEM index 3 in Fig. 12. Matchups of these database entries with the corresponding physical emissivity model conditions in Fig. 12 reveals that they cover higher VWC conditions (clumped > 5 kg m^{-2}).

b. Example from GMI

To illustrate how a priori database candidates are selected “on the fly” when running the EPC retrieval with input passive

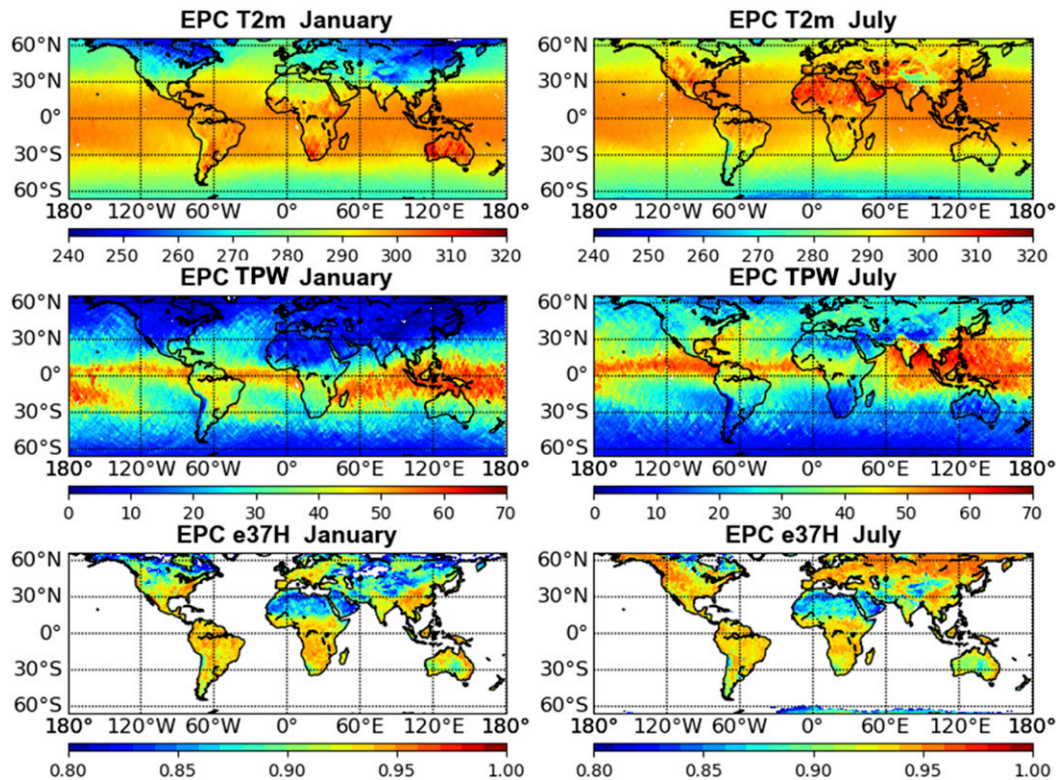


FIG. 8. Global maps of (top) the average 2-m air temperature (T2m), (middle) total column precipitable water vapor (TPW), and (bottom) horizontally polarized 37-GHz emissivity (e37H), estimated from the 5 years of GMI TB data during (left) January and (right) July. For e37H, ocean areas are masked to improve emissivity contrast.

MW radiometer data, the ascending GPM overpass over the central United States near 0043 UTC 8 June 2018 is used for an example. While other locations (over-ocean, coastal or mixed pixels, etc.) could be used, here the central United States was selected since in general the dense vegetation cover sharply decreases westward of 100°W longitude. Consequently, it is an appropriate area to examine an automated capability of the retrieval scheme to adapt to variable vegetation surface conditions.

One of the diagnostic fields produced by the EPC retrieval is the locations of the top-ranked database entries for each pixel. The ranking is done by ordering (from smallest to largest) the root-mean-square (RMS) difference between the EPC vector for the input pixel and each database candidate. Figure 13 shows the locations of the top-ranked database entries for the GMI pixel closest to 36°N, 98°W, where the symbol color indicates the 3-month interval. The locations largely cluster in the summer months in southern Madagascar, northern Tanzania, and Kenya, which are known light-to-moderate vegetated areas in the African continent. Conversely, for the GMI pixel closest to 36°N, 94°W inside the Oklahoma–Arkansas border (Fig. 14), the top-ranked database candidates generally cluster in known heavy vegetated areas in Bolivia, Paraguay, and northern Zambia, which occur during the same season in the Southern Hemisphere.

As precipitation begins to occur over either of these areas, the a priori database search will gradually begin to move toward similar-surface bins that contain some precipitating scenes. Eventually, for heavy enough precipitation rates the search will move toward bins that are heavily raining, where the land surface emissivity does not significantly influence the observed TB. This is accommodated by spacing the bins at the extreme ends in logarithmic intervals. Since the extreme rain events have an EPC structure that tends to cluster at the ends (last bin), this allows the EPC search to better narrow its search to capture heavy rain events.

6. Improving precipitation detection with TB-based supervised machine learning

This class of algorithms hypothesizes that “physical similarity” between the observed or simulated brightness temperatures can be characterized through a “mathematical distance.” In other words, closer vectors of brightness temperatures, in a mathematical sense, represent a more physically consistent condition across the surface and atmospheric continuum. For example, pixel-level brightness temperatures of a snowfall profile over snow-covered tundra shall be closer to those of snowfall over grasslands than those of rainfall over woody savannas. Figure 15 provides evidence for acceptance of such a

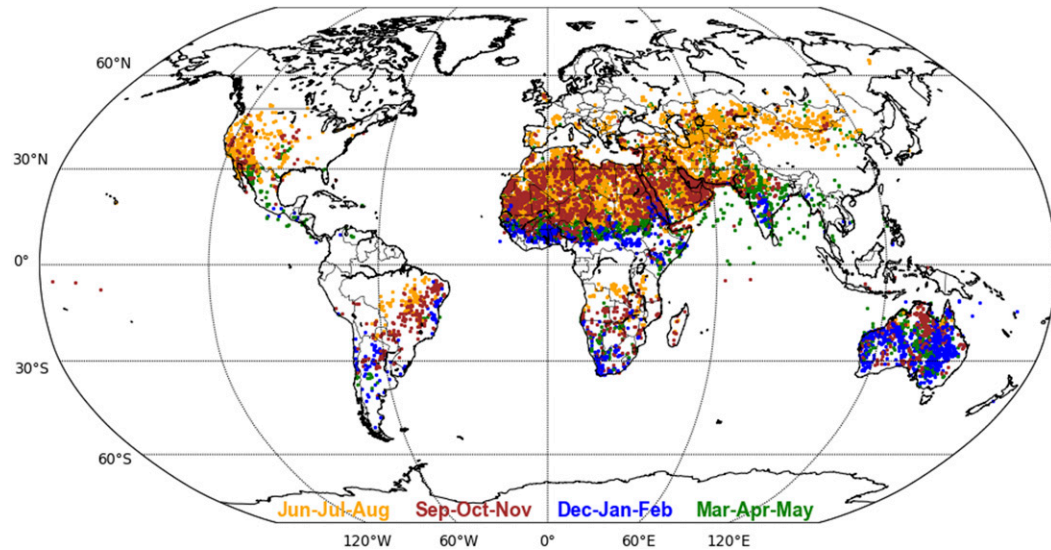


FIG. 9. Locations of entries from EPC database index 18572, corresponding to regions of light vegetation. This database represents high EPC1, low EPC2, and moderate EPC3. The symbol color indicates the 3-month period, where blue = December–February (DJF), green = March–May (MAM), orange = June–August (JJA), and brown = September–November (SON).

hypothesis showing that the nearest neighbors in vector space of TB values can isolate physically consistent rainfall profiles. These results simply demonstrate that the uncertainty of such a matching approach can be higher over land than oceans. Building on such a hypothesis, the Bayesian retrieval algorithms can be equipped with a detection step using a multi-frequency k -nearest neighbor (kNN) classification method (Ebtehaj et al. 2015, 2016).

Specifically, for an observed TB, this approach searches the entire a priori database and isolates its k -nearest neighbors

based on the Euclidean or the Mahalanobis distance. Using those nearest neighbors, the occurrence and phase of precipitation are decided based on a nested probabilistic vote rule (Takbiri et al. 2019). After detection of precipitation and its phase, statistics of the precipitation profiles corresponding to those nearest neighbors can be used for the retrieval of the precipitation profile of interest. Since all frequency channels are used, the dependencies between the surface and atmospheric emissivity values are implicitly accounted for, which makes the retrievals less sensitive to potential changes of surface emissivity.

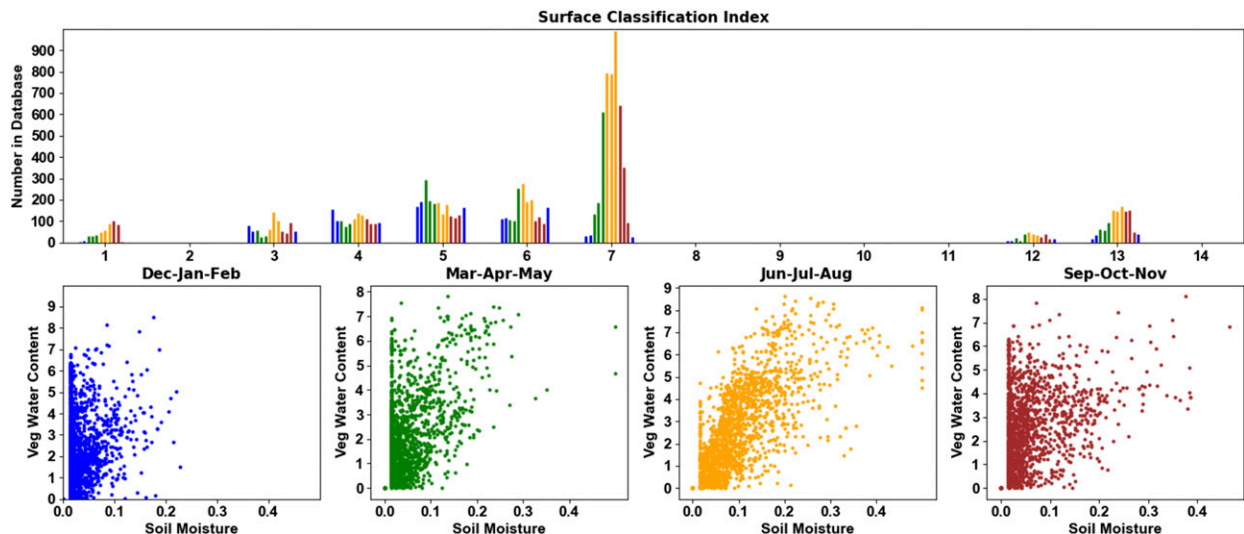


FIG. 10. (top) Histogram of the TELSEM surface classification (Table 2), for all data points shown in Fig. 10. The line color refers to the 3-month period corresponding to Fig. 9. The points cluster near class = 7, indicative of low vegetation conditions, but also some for lighter vegetation (classes 3–6). (bottom) Scatterplots of vegetation water content (kg m^{-2}) as a function of soil moisture, from the corresponding WindSat physical model. Each 3-month period (each panel) is colored by its corresponding color in Fig. 9.

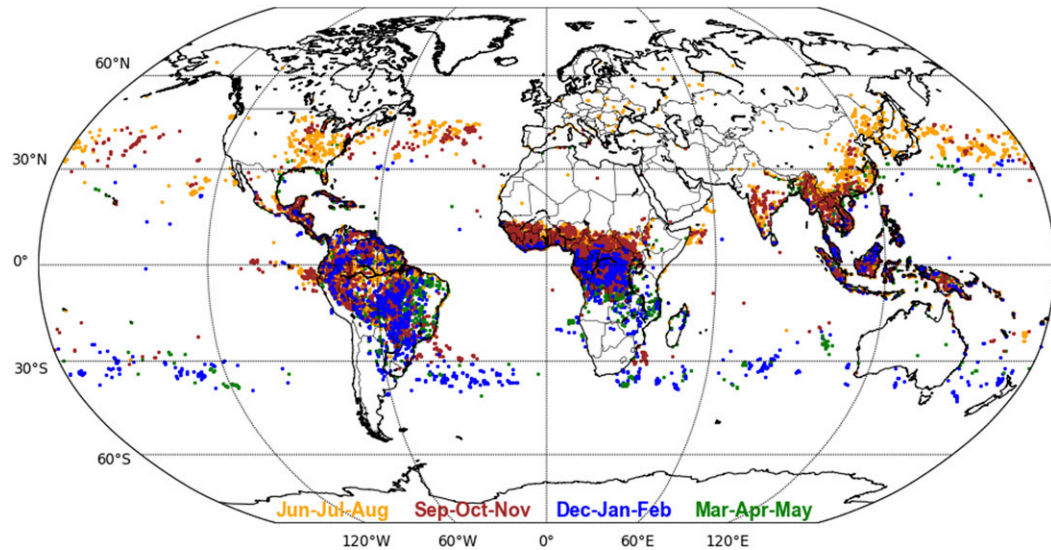


FIG. 11. As in Fig. 9, but for locations of entries from EPC database index 19146, corresponding to regions of heavy vegetation. This database represents high EPC1, high EPC2, and low EPC3.

Figure 16 compares the results of a kNN classification approach for precipitation phase detection in two different storms captured by a GPM overpasses. The classification uses a database populated with a statistically representative number of coincidences between GMI and DPR (Ebtehaj and Kummerow 2017). The storms occurred late fall and early winters in 2016 and 2015 over Lake Michigan and its southern shores, where the land surface was partly covered by snow. Due to sharp changes of near surface air temperature, ground-based radars captured occurrence of precipitation in both liquid and solid phases. The results are compared with coincident ground-based observations from the MRMS and the actual retrievals from the DPR. Over such complex and heterogeneous land surface emissivity dynamics, visual comparisons

with the MRMS data show that the kNN approach can properly retrieve precipitation occurrence and phase change without using any ancillary information about land surface emissivity and near surface air temperature. Nevertheless, it is expected that narrowing down the search for the nearest neighbors using a priori information about the land surface emissivity will significantly improve the results.

7. Frozen surface spectral signature signal for snowfall retrieval

Detection and quantification of snowfall by passive microwave observations remains among the most challenging tasks in global precipitation retrieval (Levizzani et al. 2011;

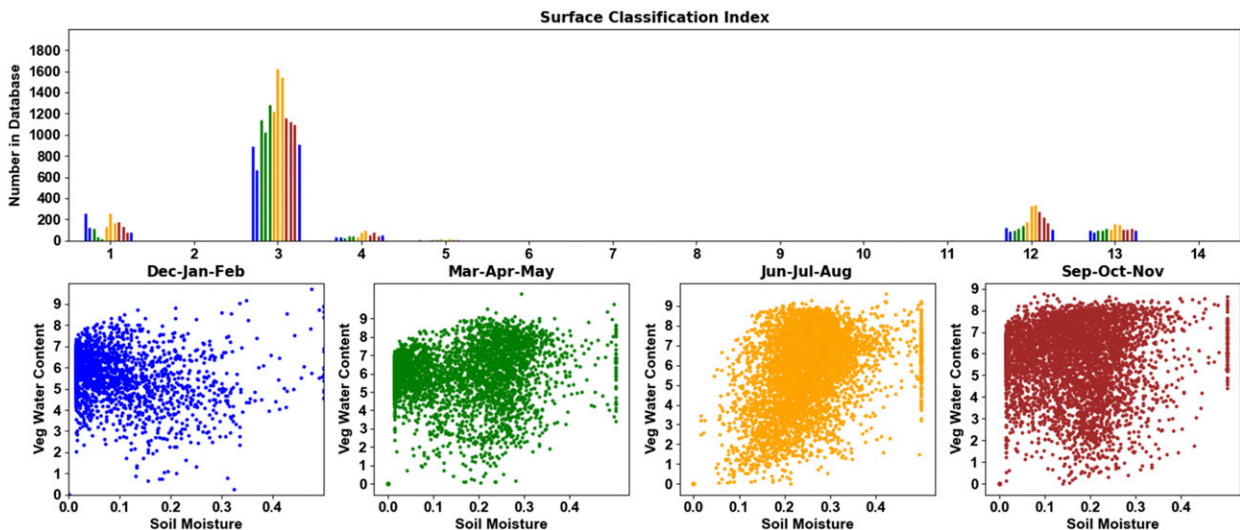


FIG. 12. As in Fig. 10, but for the data points in Fig. 11. From Table 2, these points cluster near class = 3, indicative of high-vegetation conditions.

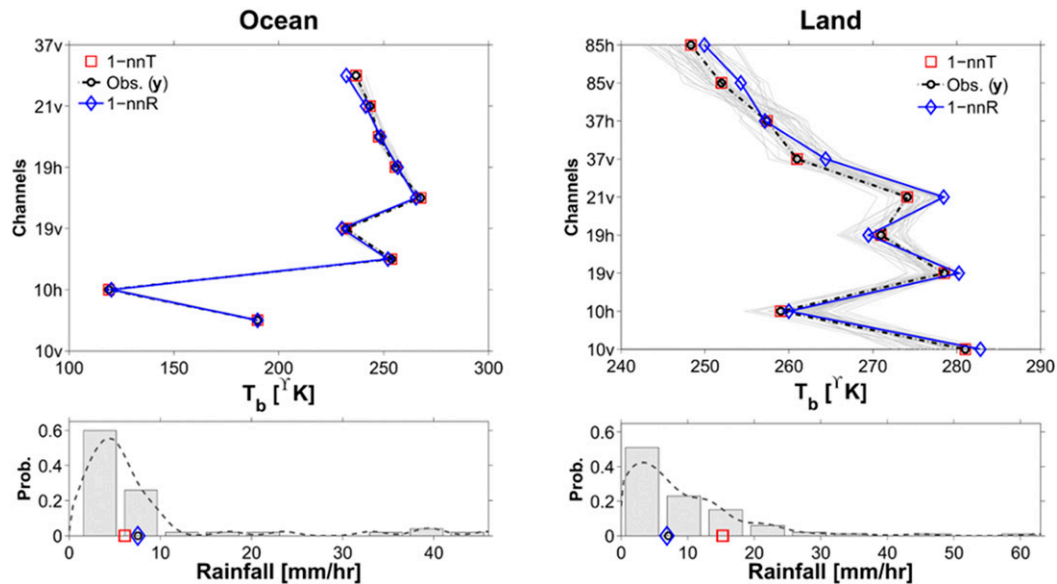


FIG. 15. (top) Two arbitrary sampled raining vectors of the TMI spectral brightness temperatures (dotted black lines with circles) over ocean and land. The gray lines are the 50-nearest neighbors using the Euclidean distance, obtained from an independent database of TMI and DPR coincidences. (bottom) Surface rainfall probability histograms of the 50 spectral neighbors shown in the top panels from PR-2A25 product (v04). In the top and bottom panels, the red squares and the blue solid lines with diamonds show the first nearest neighbor in the spectral (1-nnT) and rainfall (1-nnR) domains, respectively (Ebtehaj et al. 2015).

climatological microwave emissivity datasets (Prigent et al. 2008), often used in conjunction with daily products for snow cover extent (and sea ice concentration) (as in GPROF, see section 2). A first attempt to account for such variability has been made in a recently developed snowfall retrieval algorithm for the GMI (Snow Retrieval Algorithm for GMI, or SLALOM) (Rysman et al. 2018, 2019), based on machine learning techniques and on the use of *CloudSat*/*CALIPSO* snowfall/cloud products in the training phase, where no assumptions on the background surface are made, and where the GMI low-frequency (LF) channels (less than 95 GHz) are used to optimally exploit the snowfall-related signal at the high frequencies. SLALOM is able to predict snowfall occurrence (with and without supercooled cloud water), snow water path, and surface snowfall rate in very good agreement with the *CloudSat* CPR observations with the advantage of ensuring a much larger spatial coverage corresponding to the GMI swath.

In a recent study, Mroz et al. (2021) have carried out an extensive validation of surface snowfall rate estimates from GPM products (DPR-based products, as well as GPROF (V5) and SLALOM) and from the *CloudSat* CPR 2C-SNOWPROFILE v5 product (Wood and L’Ecuyer 2013) over the CONUS region using a 4-yr MRMS snowfall rate dataset as a reference. All of the analyzed satellite-based products tend to underestimate the intensity of the snowfall events (by 50% for the GPM products and by 30% for CPR), confirming that snowfall quantitative estimation from space is indeed a big challenge. CPR snowfall rate estimates, although by far in better agreement with the ground-based radar estimates, are affected by underestimation of intense snowfall rate due to

W-band (94 GHz) reflectivity saturation and issues related to the attenuation correction [see Battaglia and Panegrossi (2020) for a recent study on this issue]. In terms of snowfall detection, Mroz et al. (2021) show that SLALOM [with Heidke skill score (HSS) close to 60%, only 10% worse than of the CPR] outperforms the other GPM products. These authors have analyzed GPROF and SLALOM detection capabilities for different surface types, using the GPROF surface classification in Table 2. The results indicate that SLALOM is relatively stable irrespective of the land surface type (HSS varying from 63% over minimum vegetation to 58% over maximum snow cover). On the other hand, GPROF shows almost a factor of 3 difference between the lowest and the highest HSS over different surfaces, with lowest HSS (14%) reported over the maximum snow class, and higher over other snow classes (HSS around 30%–40%). The main issue in GPROF are the false alarms (60%–70% false alarm ratio. Evidently, SLALOM (with 20%–40% false alarm ratio over snow cover, 10%–20% over vegetated land), through the exploitation of all GMI channels, is able to better interpret the signal over the different surface types.

It is worth noting that GPROF (V5) uses DPR-based products in the a priori database for precipitation retrievals over all surfaces (vegetated land, inland waters, coastlines oceans, sea ice and sea ice–ocean boundaries), except for the four snow-covered surface types, where the a priori database is built from MRMS-based snowfall estimates. Therefore, for snowfall retrieval the correct identification of snow cover at the time of the GMI overpass is not only important for the surface category partitioning of the a priori database (see section 2),

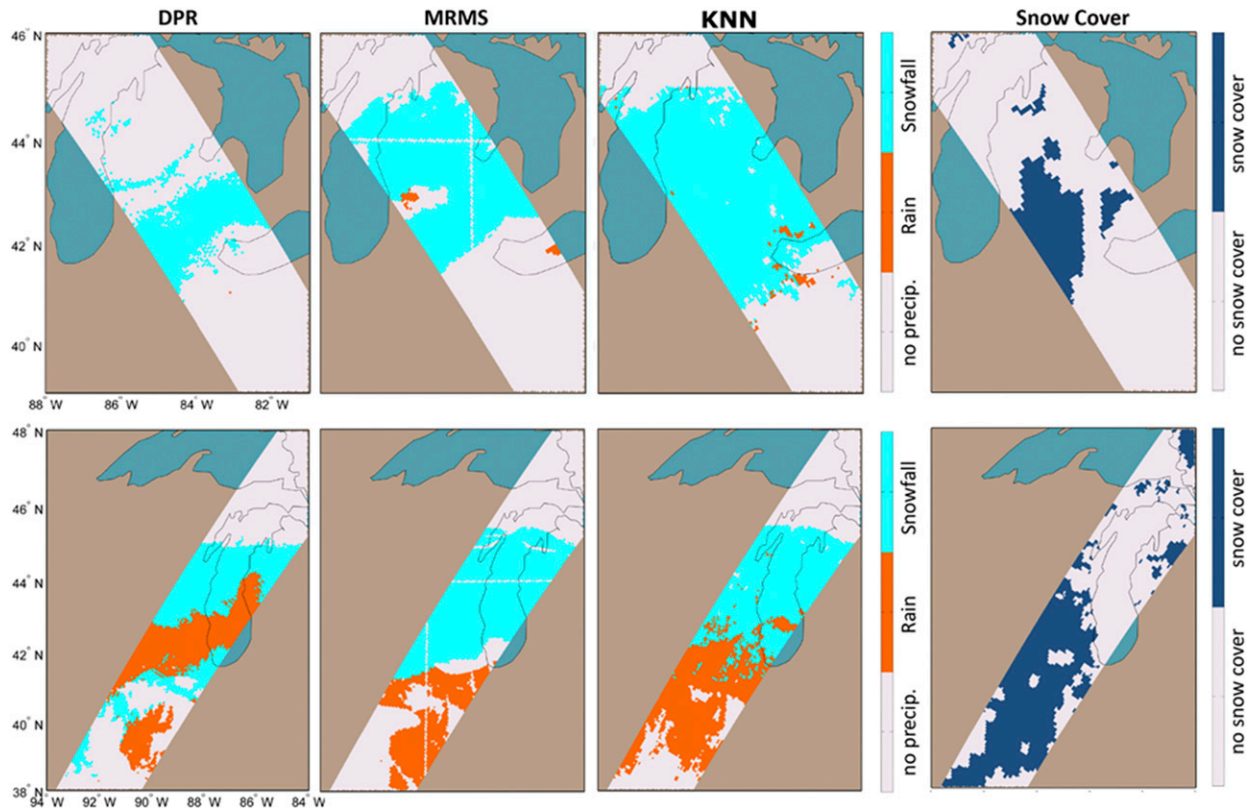


FIG. 16. Results of precipitation phase detection over snow cover for two GPM overpasses, by the standard 2A-DPR product, the ground-based Multi-Radar Multi-Sensor System (MRMS), and the proposed k -nearest neighbor (kNN) approach (Ebtehaj and Kummerow 2017). The snow-cover maps in the fourth column are from the NOAA Autosnow product (Romanov et al. 2000). (top) 21 Nov 2016, orbit 10412 and (bottom) 28 Dec 2015, orbit 9833.

but also because it determines which snowfall reference dataset is used in the retrieval process. In a recent study by Milani et al. (2020), the impact of GPROF surface classification and a priori database selection on snowfall detection and retrieval has been thoroughly analyzed. Two very intense shallow lake effect snowfall (LES) events occurring in extremely dry conditions over the U.S. Great Lakes region, were examined in detail. Both LES systems exhibit a very distinct GMI snowfall scattering signature (strong TB depression in the HF channels at 166 and 183.31 GHz) in correspondence of the most intense snowfall bands observed along the coast of Lake Ontario and Lake Erie by closest NEXRAD weather radars. The authors evidence that GPROF's ability to detect the snowfall and to capture the snowfall intensity critically depends on the GPROF background surface categorization, in particular on the correct assignment of the snow cover class to the coastal areas (based on Autosnow daily updates overwriting the monthly TELSEM-based classification, see section 2), which were affected by the most intense snowfall. The monthly surface classification, at relatively low spatial resolution, may be not suitable for coastal areas, and in general where the surface status is rapidly evolving, as in presence of seasonal snow. The use of a daily snow cover high-resolution product such as Autosnow, can sometimes mitigate this issue. However, the

subdaily snow cover variability may not be correctly represented, and the snow cover types (with different radiative properties) will be only related to the monthly climatology.

These studies evidence how critical is the influence of snow-covered surface temporal and spatial variability on the snowfall passive microwave signature, especially in dry conditions, and how it is fundamental to be able to account for such variability in the snowfall retrieval process. The passive MW empirical cold surface classification algorithm (PESCA) has been recently developed for the detection and characterization of the frozen background surface at the time of the overpass using passive MW satellite measurements, with the aim of supporting snowfall detection and retrieval (Camplani et al. 2021), especially in dry conditions. The methodology is based on the use of the lower-frequency channels (<90 GHz) common to most microwave radiometers, with the main intent to make it applicable to conically and cross-track scanning radiometers. PESCA classifies the background surface into nine classes (Fig. 17) through a series of simple tests (a decision tree) built upon an empirical method applied to observational datasets. It uses a limited number of inputs, namely, the 2-m air temperature (T_{2m}) and three tests based on TB observations. These are the ratio between the 23.8- and the 89-GHz TB (R_{LF}), the ratio between 23.8-GHz TB and 2-m air temperature

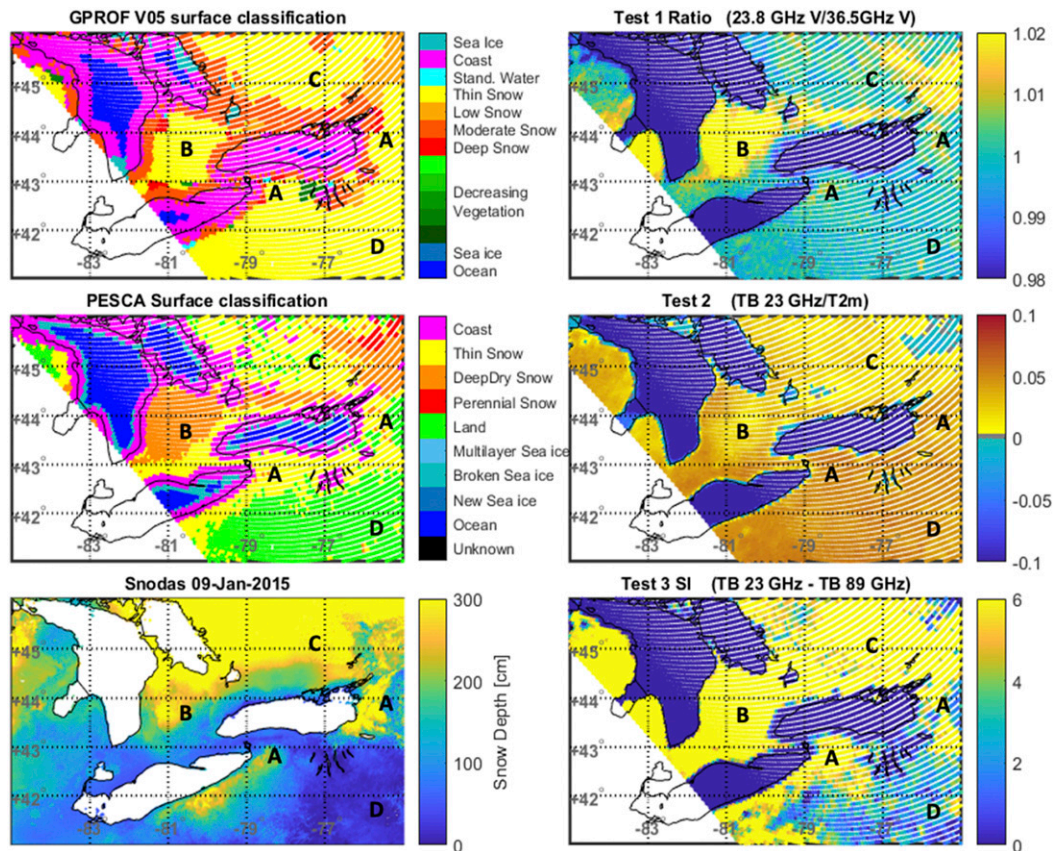


FIG. 17. GMI overpass at 1226 UTC for a lake effect snow event on 9 Jan 2015. (left) GPROF surface classification, and PESCA surface classification, and Snow Data Assimilation System [SNODAS, from the National Operational Hydrologic Remote Sensing Center (NOHRSC)] snow depth. (right) Representation of the three main tests used in the PESCA decision tree for snow cover categorization, where test 1 identifies deep dry snow, test 2, perennial snow, and test 3 thin snow (where the first two tests fail). The input variables used for each test are indicated on top of each panel.

($TB_{23.8}/T2m$), and the scattering index (SI), calculated here as the difference between the (V-polarization) TB at/near 90 and 23.8 GHz. These channels are available from most sensors (e.g., GMI, AMSR-2, SSMIS, ATMS) (Table 1). These are referred to below as test 1, test 2, and test 3, respectively. Unlike the four decreasing snow classes used in Table 2, PESCA is able to distinguish between various classes of snow and sea ice, besides coast, snow-free land, and ice-free ocean. In particular over land at midlatitudes, snow cover is further distinguished as “deep dry snow” and “thin snow,” while “perennial snow” is found mostly at higher latitudes. Camplani et al. (2021) show that PESCA has very good snow cover detection capabilities in dry conditions, when $TPW < 10$ mm, for $T2m < 270$ K and for surface elevation (averaged over the radiometer instantaneous field of view, IFOV) less 2500 m, especially for deep dry snow and perennial snow. The algorithm tends to miss thin snow with spectral signature very similar to snow-free land, while false alarms are mostly related to thin snow at $T > 270$ K. The geographical and seasonal distribution of the PESCA snow classes is coherent with previous studies (Takbiri et al. 2019; Munchak et al. 2020) and

tend to correspond to different snow physical properties (e.g., snow water equivalent, SWE). Most importantly (since the main target of PESCA is to identify distinct surface emissivity spectra), the first two classes show distinctive spectral features: “deep dry snow” is polarized and characterized by generally lower emissivity and by a steep decrease of the emission spectrum between 19 and 90 GHz, whereas “thin snow” is found in correspondence of higher $T2m$, and shows high emissivity at all frequencies below 90 GHz and low emissivity above 90 GHz.

Figure 17 shows an example of application of PESCA to one LES event (Milani et al. 2020), which occurred on 9 January 2015 (GMI orbit 4914) over the Great Lakes in extremely dry conditions (TPW around 4 mm). The left panels of Fig. 17 show the GPROF surface classification index, the corresponding PESCA surface classification, and the Snow Data Assimilation System (SNODAS) (Carroll et al. 2006) snow depth for the same day. The panels on the right present the main input variables of PESCA’s decision tree. GPROF assigns snow cover almost everywhere, except for the inner part of the lakes and the coastal areas south of Lake Ontario and Lake Erie. In

contrast, PESCA classifies the extended region labeled as D as snow-free land, where SNODAS reports very thin snow. The intense (shallow) LES snow bands occurred mostly in the two areas labeled as A (see Milani et al. 2020). In this area SNODAS reports moderate (up to 300 cm) snow depth and is identified by PESCA as thin snow. In GPROF, this area is assigned mainly to the coast class, and all the surrounding areas are assigned to moderate or low snow (class 9 or 10 in Table 2) by GPROF. PESCA instead reports mostly thin snow around the Lakes (and some broken sea ice on the lakes' shore). In regions B and C, GPROF assigns thin snow (class 11 in Table 2), while PESCA detects deep dry snow in area B, while in C a mixture of various snow types (mostly deep dry snow, thin snow, and some perennial snow) and scattered areas of snow-free land are found. SNODAS, instead, reports deep snow in both regions. As opposed to region D, region C is characterized by dense needleleaf evergreen forest that probably masks the signal from the deep snow. The right panels of Fig. 17 show the input variables used by PESCA to highlight some spectral characteristics of the snow surfaces identified by the algorithm. The deep dry snow identified in area B and C is characterized by $R_{LF} > 1.01$ (test 1) in the top right panel, while the small areas of perennial snow in area C (light blue pixels in the northeastern corner of the middle-right panel) are identified with the TB at 23.8 GHz (test 2). The test on the scattering index (test 3, bottom-right panel) is applied to areas, where the two previous tests fail. This last test identifies the thin snow if the $SI > 5$ K.

The PESCA surface categories have been used to compute the clear sky TB, for this case study, in order to separate the signal due to the presence of clouds from that due to snow cover. First, the surface emissivities have been computed based on the *CloudSat*–GPM coincidence dataset 2B-CSATGPM V03B (Turk et al. 2021, manuscript submitted to *Remote Sens.*), where each GMI observation is associated to PESCA snow cover class, and where the CPR cloud mask has been used to remove observations with cloud cover. A δ -Eddington radiative transfer code, applied using ERA5 temperature, water vapor profiles, and skin temperature, and the GMI observed TB have been used to retrieve the 13 GMI channels emissivity (emissivity spectrum) for every clear-sky observation in the dataset. Then, all observations in the dataset have been grouped based on PESCA surface class (the nine classes shown in Fig. 17) and 5-K T2m bins, and the mean emissivity in each T2m bin has been calculated. Then, for each pixel in the case study, the emissivity spectrum for each surface class has been used in a δ -Eddington radiative transfer model, in order to calculate the clear sky TB.

Figure 18 shows the TB measured by GMI at 166 GHz (V pol) and 183 ± 7 GHz, the most suitable to identify shallow snowfall signature according to Milani et al. (2020), and the corresponding Δ TB (i.e., measured minus clear sky TBs) for the same channels. Using the measured TB alone, it is difficult to discriminate between clouds and snow-covered surfaces, as some snow areas with low emissivity (e.g., area B with deep dry snow) can be easily misinterpreted. The Δ TBs shows instead relatively strong TB depressions at 166 GHz (Δ TBs down to -20 K) due to the scattering from the most intense

snowfall regions, less evident scattering signature over Lake Ontario, and TB enhancement at 166 GHz (less evident at 183 ± 7 GHz) in area B. This may be attributed to supercooled cloud water emission (MRMS observes some scattered area of snowfall in that region, see Milani et al. 2020), over the radiatively cold deep dry snow. The Δ TBs show also some features that can be attributed to the surface emissivity computation. For example, in area C the positive Δ TBs could be partly related to the not correct surface characterization (evergreen forests), while along the shore of the lakes it is related to the uncertainty of the surface emissivity over water–ice–land boundaries.

This case study is used as a proof of concept of the potentials (and limitation) of using the frozen surface characterization at the time of the overpass, and of Δ TBs (measured-clear sky) for snowfall retrieval. The Δ TBs can play a role similar to the polarization corrected temperatures (PCTs) usually applied to enhance the precipitation signature over ocean–land boundaries. The Δ TBs could be used, in principle, over all surfaces, and can be particularly useful over dry snow cover. Deep dry snow is characterized by significant volume scattering (low emissivity), that, especially in dry conditions (TPW < 5 mm), makes it very difficult for the PMW retrieval algorithm to identify snowfall scattering signature at frequencies > 89 GHz. TB depression with respect to clear sky could be a useful input parameter for snowfall retrieval. Moreover, the warming effect by cloud liquid water (embedded or at the cloud top) may result in an emission signal (TB increase) at frequencies > 89 GHz, that, if correctly interpreted, could indicate the likelihood of snowfall.

8. Leveraging the spatial patterns of brightness temperature to separate the surface and precipitation

When considered at the pixel level, multispectral TB signatures are generally ambiguous because they are the product of both the surface's emission and the atmospheric contribution. To help separate the two signals, other than utilizing ancillary information, one can leverage the spatial dynamics and patterns in the observed TB fields. Indeed, the variations of TB coming the variations of the surface properties and the variations caused by hydrometeors occur at different spatial scales and show different spatial dynamics, leading to distinguishable spatial patterns. In Guilloteau and Foufoula-Georgiou (2020) it is demonstrated that over oceans, adequate spatial filtering helps distinguish ice scattering signal from liquid rain drops emission signal at 37 and 89 GHz. Over land, the signal associated to ice scattering in a convective cell at frequencies between 15 and 200 GHz generally corresponds to a local depression of the TB. The specific scale of an individual convective cell over land is typically smaller than $50 \text{ km} \times 50 \text{ km}$. The spatial dimensions of the corresponding TB depression tend to decrease with frequency, as the lower frequencies are only sensitive to the largest ice particles present in the very core of the convective cells. The TB depressions caused by convective cells are generally shaped as disks or elliptical disks with low eccentricity. All these geometrical characteristics make the signature of convective cells relatively easy to

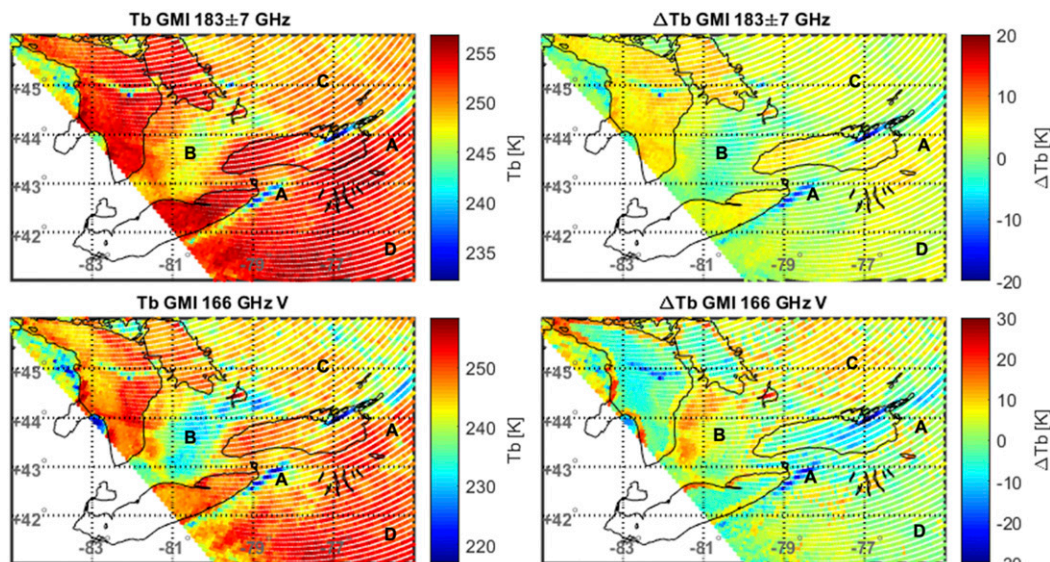


FIG. 18. GMI overpass at 1226 UTC for a lake effect snow event on 9 Jan 2015. Comparison of the (left) TB measured by GMI at 183 ± 7 GHz and 166 GHz and (right) the TB differences, between measured TBs and the clear sky TBs. The clear sky TBs have been calculated from the mean emissivity for the corresponding PESCA surface category (see text for details).

identify and distinguish from other sources of variability for the human eye analyzing TB fields.

The challenge for precipitation retrieval algorithms is to find the operators able to extract useful spatial patterns from the TB fields. Figure 19 shows the average spatial pattern observed by GMI for 11 747 convective cells over land at 18.7, 37, 89, and 166 GHz. The presence of a convective cell for each one of the 11 747 cases is established through the collocated DPR observations. TB patches of dimensions $55 \text{ km} \times 65 \text{ km}$ centered on each cell are extracted and averaged at each frequency. One will note the asymmetry of the patterns in the cross-scan direction. This asymmetry is not a property of the precipitation system themselves but comes from the observation geometry of GMI, which involves a 53° Earth incidence angle and results in a frequency-dependent parallax shift in the cross-scan direction (Guiloteau et al. 2018; Guiloteau and Foufoula-Georgiou 2020). In general, the deeper the convection, the more pronounced the parallax shift and the asymmetry. The geometrical distortions resulting from the Earth incident angle of conical-scanning imagers are often considered as a deteriorating factor for precipitation retrievals, but in fact, they result in specific patterns that can be exploited to recognize and characterize specific atmospheric features and differentiate the atmospheric signal from the surface signal. The patterns shown in Fig. 19, corresponding to the “average” spatial signature of a convective cell, may be used as convolution kernels to identify convective cells in the TB fields.

However, these simple average patterns may not capture well the variability in terms of spatial organization and microphysical properties across different convective cells. In Guiloteau and Foufoula-Georgiou (2020), spatial filtering of the 37- and 89-GHz TBs with a local derivative operator was

found to allow extracting information capable of improving the retrieval of precipitation over land. A promising approach for identifying relevant TB patterns for precipitation retrieval is machine learning through deep neural networks as these have allowed major breakthroughs in the field of image recognition in the past two decades (LeCun et al. 2015).

9. Conclusions

This manuscript has described several recent developments to passive MW overland precipitation retrieval algorithms that have resulted from the availability of the GPM core radar (DPR) and radiometer (GMI) and other GPM constellation radiometers. In general, these findings point to the importance of adapting to the surface emissivity conditions and the large-scale environmental conditions that exist near the time of the satellite observation. For the Bayesian-based algorithms, knowledge of these conditions better isolates and constrains the selection of candidate precipitation profiles from the large collection of a priori data.

Even with their coarser resolution relative to the higher-frequency channels, incorporation of passive MW channels at 37 GHz and below, especially channels with a polarization capability, clearly improve the overland estimates. These channels help to better separate and discriminate the variable surface conditions and the precipitation above. This is an important consideration for precipitation estimates based on the abundant observations from the high-frequency passive MW sounders (e.g., AMSU-B, ATMS, MHS, and future systems such as MWS on *MetOp-SG-A*), which also have channels at/near 23 and 31 GHz.

The narrow-swath precipitation radars on board TRMM and GPM also serve to separate the precipitating and nonprecipitating

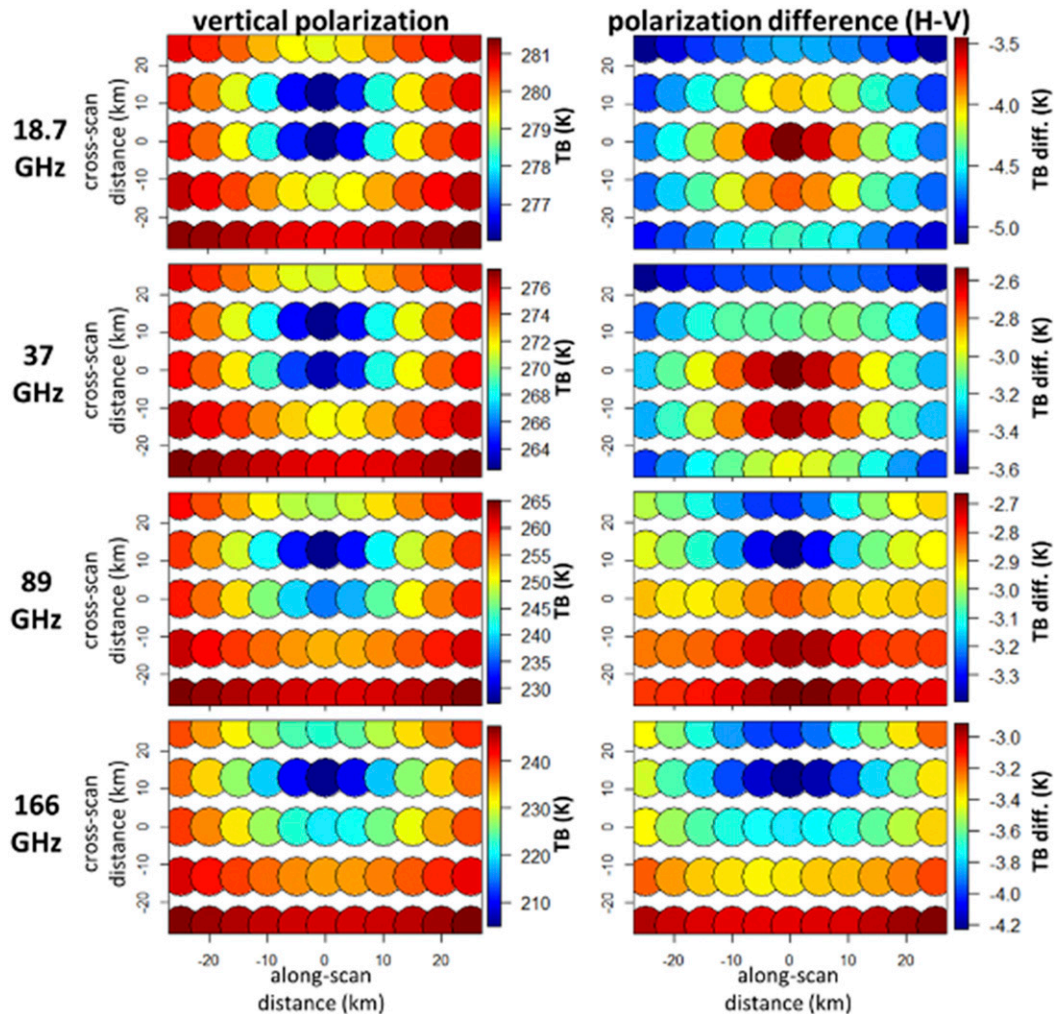


FIG. 19. Average TB pattern at 18.7, 37, 89, and 166 GHz observed by GMI for 11 747 convective cells over land (vegetated surfaces). Each one of the 11 747 averaged TB patches is centered on a convective cell identified by the DPR. (left) The vertical polarization TB and (right) the polarization difference ($H - V$).

passive MW observations from the GPM constellation radiometers. Using this capability, semiempirical approaches that are designed to reproduce the observed DPR precipitation products perform quite well. The EPC method eliminates surface classification, using the emissivity principal component structure for constructing and interrogating the a priori dataset. This method has demonstrated to transition across oceanic, land, and the complex nature of mixed land-water scenes with minimal surface-related artifacts in the resultant precipitation structure (Utsumi et al. 2020). These techniques require sufficient collection of a passive MW sensor together with a precipitation radar (PR or DPR) to build the a priori dataset.

An advantage of simulated TB data is that any passive MW sensor can be modeled, including future sensors not yet deployed, to design future algorithms and collect a large volume of simulated a priori precipitation data. To effectively model the overland TB for future passive MW sensors,

forward-modeled TB simulations (initialized with the precipitation radar microphysics) are needed. This highlights the broader need to further integrate the land surface into atmospheric radiative transfer models to more accurately model TB across land surface conditions (Ringerud et al. 2015).

While there has been improvement to the quantification of cold-season precipitation and snow-covered surfaces, there are complex surface-atmosphere interactions that are challenging to disentangle even with the capabilities of the DPR and high-frequency radiometer channels. High-frequency radar observations such as *CloudSat* and future radars (Battaglia et al. 2020), even if they are not coincident with DPR, have abundant fortuitous coincidences with DPR and the polar-orbiting passive MW sensors at the high latitudes (Hayden and Liu 2018). Despite the sampling and spatial resolution differences, joint *CloudSat*-passive MW observations have guided the capability to better detect the light end of the precipitation rate with the numerous passive MW sounders (Behrangi et al. 2014).

Even with the increased radar sensitivity in this precipitation regime, challenges remain in estimating light rain over land surfaces (Mitrescu et al. 2010). Finer spatial/temporal-scale numerical weather prediction data to define the atmospheric and land surface state can better guide the estimation.

With the abundance of passive MW high-frequency sounder data in the GPM era, much of the area poleward of 60° latitude has revisit times of 3 h or less. The complex surface emissivity properties at these latitudes can be circumvented to some extent by utilizing TB time-change methods to estimate the nonprecipitating background TB, to mitigate the surface contamination and improve rainfall retrieval performance. This approach has the potential to augment the GPROF land precipitation retrieval algorithm by including the “time dimension” into the retrieval process. On the other hand, current passive MW retrievals are based on a “per pixel” retrieval; i.e., the spatial characteristics of the precipitation as revealed in the TB patterns are not taken into account. Operators that introduce the “spatial dimension” into the retrieval process hold promise to differentiate the atmospheric signal from the surface signal (Guiloteau and Foufoula-Georgiou 2020).

This manuscript has intentionally focused on passive MW-only precipitation algorithms. However, the variable nature of the microwave land surface properties also affects the CORRA algorithm for TRMM and GPM (Greco et al. 2016), by introducing uncertainties in the relationship between the radar surface backscatter cross section and the surface emissivity (Munchak et al. 2020). Since the CORRA precipitation profile is used in the a priori data used for many passive MW precipitation methods highlighted here, any surface-induced precipitation characteristics within CORRA eventually manifest themselves in subsequent multisatellite (Level 3) IMERG products.

Looking ahead, there are several promising methods not covered in this manuscript. The methods described have all operated on the principle of discriminating precipitation against a high-emissivity land surface at the time of the satellite overpasses. Conversely, the relative change in the surface emissivity can be related to the amount and duration of precipitation that impacts the surface *prior* to the satellite overpass (You et al. 2014). When rain impacts the surface, the surface emissivity of many soils changes dramatically owing to the strong contrast between the permittivity of dry and wet soil types, especially at C-band frequencies (5 GHz) and below. This principle has guided the development of antecedent precipitation estimates from other active/passive satellite observations that are sensitive to soil moisture change. These include, but are not limited to observations from microwave scatterometers (Brocca et al. 2014; Turk et al. 2015), L-band (1.4 GHz) radiometers such as SMOS and SMAP (Brocca et al. 2020), and the expanding collection of L-band land surface reflection data from Global Navigation Satellite System (GNSS) telemetries (Wan et al. 2019) and other signals of opportunity (Edokossi et al. 2020).

The highly nonlinear and multidimensional nature of the MW surface emissivity is a highly under constrained problem when working with the limited set of passive MW TB channels. As shown in section 6, this complexity makes this topic an

appropriate candidate for machine learning methods. Use of these techniques have been proposed for satellite-based precipitation estimation for many years (Tapiador et al. 2004), but have evolved with computational advances, readily available tools, and more meteorological-driven insight, discovery and training methods (Ebert-Uphoff and Hilburn 2020; Boukabara et al. 2019). These methods may help to identify connections between physical properties that are not represented in current physical emissivity models, and improved utilization of the high-frequency MW sounder data (Sanò et al. 2015). Current initiatives are largely focused on improved Level 3 precipitation products, especially incorporating surface and topographical features (Bhuiyan et al. 2020), but also to improve the quality of instantaneous passive MW estimates (Petković et al. 2019) and MW-IR estimates in the high latitudes (Tang et al. 2018).

Acknowledgments. The authors acknowledge the support from NASA under the Precipitation Measurements Mission (PMM) science team. NU acknowledges support from JSPS KAKENHI Grant Number JP19K15096 and KUAS Interdisciplinary Research Activity Support. YYL would like to thank the support from NASA Grant 80NSSC20K0903 from the Weather and Atmospheric Dynamics program. GP, PS and DC would like to thank the support from the RainCast study (ESA Contract 4000125959/18/NL/NA) and from the EUMETSAT Satellite Application Facility for Operational Hydrology and Water management (H SAF) Third Continuous and Operations Phase (CDOP-3). AC is supported by the Ph.D. program in Infrastructures, Transport Systems and Geomatics at the Department of Civil, Constructional, and Environmental Engineering at Sapienza University of Rome. The PMM Research Program is acknowledged for supporting H SAF and GPM scientific collaboration through the approval of the no-cost proposal “H SAF and GPM: Precipitation algorithm development and validation activity.” These efforts were developed under the auspices of the PMM Land Surface Working Group (LSWG), one of several working groups tasked with investigating specific aspects of the PMM precipitation algorithms. The efforts from the NASA Precipitation Processing System (PPS) for the production and distribution of the GPM constellation datasets is gratefully acknowledged. The work by FJT was carried out at the Jet Propulsion Laboratory, California Institute of Technology, under a contract with NASA.

Data availability statement. All TRMM and GPM data used here are available online from the NASA Precipitation Processing System (PPS) at <https://storm.pps.eosdis.nasa.gov/storm/>.

REFERENCES

- Aires, F., C. Prigent, F. Bernardo, C. Jiménez, R. Saunders, and P. Brunel, 2011: A Tool to Estimate Land-Surface Emissivities at Microwave frequencies (TELSEM) for use in numerical weather prediction. *Quart. J. Roy. Meteor. Soc.*, **137**, 690–699, <https://doi.org/10.1002/qj.803>.
- Battaglia, A., and G. Panegrossi, 2020: What can we learn from the CloudSat radiometric mode observations of snowfall over the

- ice-free ocean? *Remote Sens.*, **12**, 3285, <https://doi.org/10.3390/rs12203285>.
- , and Coauthors, 2020: Spaceborne cloud and precipitation radars: Status, challenges, and ways forward. *Rev. Geophys.*, **58**, e2019RG000686, <https://doi.org/10.1029/2019RG000686>.
- Behrangi, A., Y. Tian, B. H. Lambriksen, and G. L. Stephens, 2014: What does CloudSat reveal about global land precipitation detection by other spaceborne sensors? *Water Resour. Res.*, **50**, 4893–4905, <https://doi.org/10.1002/2013WR014566>.
- Bennartz, R., and P. Bauer, 2003: Sensitivity of microwave radiances at 85–183 GHz to precipitating ice particles. *Radio Sci.*, **38**, 40–41, <https://doi.org/10.1029/2002RS002626>.
- Berg, W., and Coauthors, 2016: Intercalibration of the GPM microwave radiometer constellation. *J. Atmos. Oceanic Technol.*, **33**, 2639–2654, <https://doi.org/10.1175/JTECH-D-16-0100.1>.
- Bhuiyan, M. A. E., F. Yang, N. K. Biswas, S. H. Rahat, and T. J. Neelam, 2020: Machine learning-based error modeling to improve GPM IMERG precipitation product over the Brahmaputra river basin. *Forecasting*, **2**, 248–266, <https://doi.org/10.3390/forecast2030014>.
- Boukabara, S. A., and Coauthors, 2011: MiRS: An all-weather 1DVAR satellite data assimilation and retrieval system. *IEEE Trans. Geosci. Remote Sens.*, **49**, 3249–3272, <https://doi.org/10.1109/TGRS.2011.2158438>.
- , V. Krasnopolsky, J. Q. Stewart, E. S. Maddy, N. Shahroudi, and R. N. Hoffman, 2019: Leveraging modern artificial intelligence for remote sensing and NWP: Benefits and challenges. *Bull. Amer. Meteor. Soc.*, **100**, ES473–ES491, <https://doi.org/10.1175/BAMS-D-18-0324.1>.
- Brocca, L., and Coauthors, 2014: Soil as a natural rain gauge: Estimating global rainfall from satellite soil moisture data. *J. Geophys. Res.*, **119**, 5128–5141, <https://doi.org/10.1002/2014JD021489>.
- , C. Massari, T. Pellarin, P. Filippucci, L. Ciabatta, S. Camici, Y. H. Kerr, and D. Fernández-Prieto, 2020: River flow prediction in data scarce regions: Soil moisture integrated satellite rainfall products outperform rain gauge observations in West Africa. *Sci. Rep.*, **10**, 12517, <https://doi.org/10.1038/s41598-020-69343-x>.
- Byrne, M. P., and P. A. O’Gorman, 2015: The response of precipitation minus evapotranspiration to climate warming: Why the “wet-get-wetter, dry-get-drier” scaling does not hold over land. *J. Climate*, **28**, 8078–8092, <https://doi.org/10.1175/JCLI-D-15-0369.1>.
- Bytheway, J. L., and C. D. Kummerow, 2010: A physically based screen for precipitation over complex surfaces using passive microwave observations. *IEEE Trans. Geosci. Remote Sens.*, **48**, 299–313, <https://doi.org/10.1109/TGRS.2009.2027434>.
- Camplani, A., D. Casella, P. Sanò, and G. Panegrossi, 2021: The Passive Microwave Empirical Frozen Surface Classification Algorithm (PESCA): Application to GMI and ATMS. *J. Hydrometeorol.*, **22**, 1727–1744, <https://doi.org/10.1175/JHM-D-20-0260.1>.
- Cao, C., M. Weinreb, and H. Xu, 2004: Predicting simultaneous nadir overpasses among polar-orbiting meteorological satellites for the intersatellite calibration of radiometers. *J. Atmos. Oceanic Technol.*, **21**, 537–542, [https://doi.org/10.1175/1520-0426\(2004\)021<0537:PSNOAP>2.0.CO;2](https://doi.org/10.1175/1520-0426(2004)021<0537:PSNOAP>2.0.CO;2).
- Carroll, T., D. Cline, C. Olheiser, A. Rost, A. Nilsson, G. Fall, C. Bovitz, and L. Li, 2006: NOAA’s national snow analyses. *Proc. 74th Annual Meeting of the Western Snow Conf.*, Las Cruces, NM, Western Snow Conference, 14 pp., https://www.nohrsc.noaa.gov/technology/pdf/WSC_2006.pdf.
- Casella, D., and Coauthors, 2013: Transitioning from CRD to CDRD in Bayesian retrieval of rainfall from satellite passive microwave measurements: Part 2. Overcoming database profile selection ambiguity by consideration of meteorological control on microphysics. *IEEE Trans. Geosci. Remote Sens.*, **51**, 4650–4671, <https://doi.org/10.1109/TGRS.2013.2258161>.
- , G. Panegrossi, P. Sanò, L. Milani, M. Petracca, and S. Dietrich, 2015: A novel algorithm for detection of precipitation in tropical regions using PMW radiometers. *Atmos. Meas. Tech.*, **8**, 1217–1232, <https://doi.org/10.5194/amt-8-1217-2015>.
- de Rosnay, P., J. Muñoz-Sabater, C. Albergel, L. Isaksen, S. English, M. Drusch, and J.-P. Wigneron, 2020: SMOS brightness temperature forward modelling and long term monitoring at ECMWF. *Remote Sens. Environ.*, **237**, 111424, <https://doi.org/10.1016/j.rse.2019.111424>.
- Ebert-Uphoff, I., and K. Hilburn, 2020: Evaluation, tuning and interpretation of neural networks for working with images in meteorological applications. *Bull. Amer. Meteor. Soc.*, **101**, E2149–E2170, <https://doi.org/10.1175/BAMS-D-20-0097.1>.
- Ebtehaj, A. M., and C. D. Kummerow, 2017: Microwave retrievals of terrestrial precipitation over snow covered surfaces: A lesson from the GPM satellite. *Geophys. Res. Lett.*, **44**, 6154–6162, <https://doi.org/10.1002/2017GL073451>.
- , R. L. Bras, and E. Foufoula-Georgiou, 2015: Shrunk locally linear embedding for passive microwave retrieval of precipitation. *IEEE Trans. Geosci. Remote Sens.*, **53**, 3720–3736, <https://doi.org/10.1109/TGRS.2014.2382436>.
- , —, and —, 2016: Evaluation of ShARP passive rainfall retrievals over snow-covered land surfaces and coastal zones. *J. Hydrometeorol.*, **17**, 1013–1029, <https://doi.org/10.1175/JHM-D-15-0164.1>.
- , C. D. Kummerow, and F. J. Turk, 2020: Metric learning for approximation of microwave channel error covariance: Application for satellite retrieval of drizzle and light snowfall. *IEEE Trans. Geosci. Remote Sens.*, **58**, 903–912, <https://doi.org/10.1109/TGRS.2019.2941682>.
- Edel, L., J. F. Rysman, C. Claud, C. Palerme, and C. Genthon, 2019: Potential of passive microwave around 183 GHz for snowfall detection in the Arctic. *Remote Sens.*, **11**, 2200, <https://doi.org/10.3390/rs11192200>.
- Edokossi, K., A. Calabia, S. Jin, and I. Molina, 2020: GNSS-reflectometry and remote sensing of soil moisture: A review of measurement techniques, methods, and applications. *Remote Sens.*, **12**, 614, <https://doi.org/10.3390/rs12040614>.
- Ferraro, R. R., F. Weng, N. C. Grody, and L. Zhao, 2000: Precipitation characteristics over land from the NOAA-15 AMSU sensor. *Geophys. Res. Lett.*, **27**, 2669–2672, <https://doi.org/10.1029/2000GL011665>.
- , and Coauthors, 2013: An evaluation of microwave land surface emissivities over the continental United States to benefit GPM-era precipitation algorithms. *IEEE Trans. Geosci. Remote Sens.*, **51**, 378–398, <https://doi.org/10.1109/TGRS.2012.2199121>.
- Ford, T. W., S. M. Quiring, B. Thakur, R. Jogineedi, A. Houston, S. Yuan, A. Kalra, and N. Lock, 2018: Evaluating soil moisture–precipitation interactions using remote sensing: A sensitivity analysis. *J. Hydrometeorol.*, **19**, 1237–1253, <https://doi.org/10.1175/JHM-D-17-0243.1>.
- Gelaro, R., and Coauthors, 2017: The Modern-Era Retrospective Analysis for Research and Applications, version 2 (MERRA-2). *J. Climate*, **30**, 5419–5454, <https://doi.org/10.1175/JCLI-D-16-0758.1>.
- Gopalan, K., N.-Y. Wang, R. Ferraro, and C. Liu, 2010: Status of the TRMM 2A12 land precipitation algorithm. *J. Atmos.*

- Oceanic Technol.*, **27**, 1343–1354, <https://doi.org/10.1175/2010JTECHA1454.1>.
- Gouweleeuw, B. T., A. I. J. M. van Dijk, J. P. Guerschman, P. Dyce, and M. Owe, 2012: Space-based passive microwave soil moisture retrievals and the correction for a dynamic open water fraction. *Hydrol. Earth Syst. Sci.*, **16**, 1635–1645, <https://doi.org/10.5194/hess-16-1635-2012>.
- Grecu, M., and Coauthors, 2016: The GPM combined algorithm. *J. Atmos. Oceanic Technol.*, **33**, 2225–2245, <https://doi.org/10.1175/JTECH-D-16-0019.1>.
- Grody, N. C., 1991: Classification of snow cover and precipitation using the Special Sensor Microwave Imager. *J. Geophys. Res.*, **96**, 7423–7435, <https://doi.org/10.1029/91JD00045>.
- Guilloteau, C., and E. Foufoula-Georgiou, 2020: Beyond the pixel: Using patterns and multiscale spatial information to improve the retrieval of precipitation from spaceborne passive microwave imagers. *J. Atmos. Oceanic Technol.*, **37**, 1571–1591, <https://doi.org/10.1175/JTECH-D-19-0067.1>.
- , —, C. D. Kummerow, and V. Petković, 2018: Resolving surface rain from GMI high-frequency channels: Limits imposed by the three-dimensional structure of precipitation. *J. Atmos. Oceanic Technol.*, **35**, 1835–1847, <https://doi.org/10.1175/JTECH-D-18-0011.1>.
- Haddad, Z. S., R. C. Sawaya, S. Kacimi, O. O. Sy, F. J. Turk, and J. Steward, 2017: Interpreting millimeter-wave radiances over tropical convective clouds. *J. Geophys. Res.*, **122**, 1650–1664, <https://doi.org/10.1002/2016JD025923>.
- Hamada, A., and Y. N. Takayabu, 2016: Improvements in detection of light precipitation with the Global Precipitation Measurement Dual-Frequency Precipitation Radar (GPM DPR). *J. Atmos. Oceanic Technol.*, **33**, 653–667, <https://doi.org/10.1175/JTECH-D-15-0097.1>.
- Harrison, K. W., Y. Tian, C. D. Peters-Lidard, S. Ringerud, and S. V. Kumar, 2015: Calibration to improve forward model simulation of microwave emissivity at GPM frequencies over the US Southern Great Plains. *IEEE Trans. Geosci. Remote Sens.*, **54**, 1103–1117, <https://doi.org/10.1109/TGRS.2015.2474120>.
- Hayden, L., and C. Liu, 2018: A multiyear analysis of global precipitation combining CloudSat and GPM precipitation retrievals. *J. Hydrometeorol.*, **19**, 1935–1952, <https://doi.org/10.1175/JHM-D-18-0053.1>.
- Hirahara, Y., P. de Rosnay, and G. Arduini, 2020: Evaluation of a microwave emissivity module for snow covered area with CMEM in the ECMWF integrated forecasting system. *Remote Sens.*, **12**, 2946, <https://doi.org/10.3390/rs12182946>.
- Hou, A. Y., and Coauthors, 2014: The Global Precipitation Measurement mission. *Bull. Amer. Meteor. Soc.*, **95**, 701–722, <https://doi.org/10.1175/BAMS-D-13-00164.1>.
- Kidd, C., J. Tan, P.-E. Kirstetter, and W. A. Petersen, 2018: Validation of the Version 05 Level 2 precipitation products from the GPM Core Observatory and constellation satellite sensors. *Quart. J. Roy. Meteor. Soc.*, **144**, 313–328, <https://doi.org/10.1002/qj.3175>.
- Kilic, L., C. Prigent, J. Boutin, T. Meissner, S. English, and S. Yueh, 2019: Comparisons of ocean radiative transfer models with SMAP and AMSR2 observations. *J. Geophys. Res. Oceans*, **124**, 7683–7699, <https://doi.org/10.1029/2019JC015493>.
- Kneifel, S., J. Leinonen, J. Tyynelä, D. Ori, and A. Battaglia, 2020: Scattering of hydrometeors. *Satellite Precipitation Measurement*, V. Levizzani et al., Eds., Advances in Global Change Research, Vol. 67. Springer, 249–276.
- Kubota, T., S. Seto, M. Satoh, T. Nasuno, T. Iguchi, T. Masaki, J. M. Kwiatkowski, and R. Oki, 2020: Cloud assumption of precipitation retrieval algorithms for the Dual-Frequency Precipitation Radar. *J. Atmos. Oceanic Technol.*, **37**, 2015–2031, <https://doi.org/10.1175/JTECH-D-20-0041.1>.
- Kulie, M. S., R. Bennartz, T. J. Greenwald, Y. Chen, and F. Weng, 2010: Uncertainties in microwave properties of frozen precipitation: Implications for remote sensing and data assimilation. *J. Atmos. Sci.*, **67**, 3471–3487, <https://doi.org/10.1175/2010JAS3520.1>.
- Kummerow, C., W. Barnes, T. Kozu, J. Shiue, and J. Simpson, 1998: The Tropical Rainfall Measuring Mission (TRMM) sensor package. *J. Atmos. Oceanic Technol.*, **15**, 809–817, [https://doi.org/10.1175/1520-0426\(1998\)015<0809:TTRMMT>2.0.CO;2](https://doi.org/10.1175/1520-0426(1998)015<0809:TTRMMT>2.0.CO;2).
- , D. L. Randel, M. Kulie, N. Y. Wang, R. Ferraro, M. S. Joseph, and V. Petkovic, 2015: The evolution of the Goddard profiling algorithm to a fully parametric scheme. *J. Atmos. Oceanic Technol.*, **32**, 2265–2280, <https://doi.org/10.1175/JTECH-D-15-0039.1>.
- LeCun, Y., Y. Bengio, and G. Hinton, 2015: Deep learning. *Nature*, **521**, 436–444, <https://doi.org/10.1038/nature14539>.
- Levizzani, V., and S. Laviola, and E. Cattani, 2011: Detection and measurement of snowfall from space. *Remote Sens.*, **3**, 145–166, <https://doi.org/10.3390/rs3010145>.
- , and Coauthors, 2018: The activities of the international precipitation working group. *Quart. J. Roy. Meteor. Soc.*, **144**, 3–15, <https://doi.org/10.1002/qj.3214>.
- Liu, G., and E. K. Seo, 2013: Detecting snowfall over land by satellite high-frequency microwave observations: The lack of scattering signature and a statistical approach. *J. Geophys. Res.*, **118**, 1376–1387, <https://doi.org/10.1002/jgrd.50172>.
- Liu, Q., and S.-A. Boukabara, 2014: Community Radiative Transfer Model (CRTM) applications in supporting the *Suomi National Polar-orbiting Partnership (SNPP)* mission validation and verification. *Remote Sens. Environ.*, **140**, 744–754, <https://doi.org/10.1016/j.rse.2013.10.011>.
- Mega, T., and S. Shige, 2016: Improvements of rain/no-rain classification methods for microwave radiometer over coasts by dynamic surface-type classification. *J. Atmos. Oceanic Technol.*, **33**, 1257–1270, <https://doi.org/10.1175/JTECH-D-15-0127.1>.
- Meissner, T., and F. J. Wentz, 2012: The emissivity of the ocean surface between 6 and 90 GHz over a large range of wind speeds and Earth incidence angles. *IEEE Trans. Geosci. Remote Sens.*, **50**, 3004–3026, <https://doi.org/10.1109/TGRS.2011.2179662>.
- Milani, L., and Coauthors, 2020: Extreme lake-effect snow from a GPM microwave imager perspective: Observational analysis and precipitation retrieval evaluation. *J. Atmos. Oceanic Technol.*, **38**, 293–311, <https://doi.org/10.1175/JTECH-D-20-0064.1>.
- Mitrescu, C., T. L'Ecuyer, J. Haynes, S. Miller, and F. J. Turk, 2010: CloudSat precipitation profiling algorithm-model description. *J. Appl. Meteor. Climatol.*, **49**, 991–1003, <https://doi.org/10.1175/2009JAMC2181.1>.
- Mroz, K., M. Montopoli, A. Battaglia, G. Panegrossi, P. Kirtseter, and L. Baldini, 2021: Cross validation of active and passive microwave snowfall products over the continental United States. *J. Hydrometeorol.*, **22**, 1297–1315, <https://doi.org/10.1175/JHM-D-20-0222.1>.
- Munchak, S. J., and G. Skofronick-Jackson, 2013: Evaluation of precipitation detection over various surfaces from passive microwave imagers and sounders. *Atmos. Res.*, **131**, 81–94, <https://doi.org/10.1016/j.atmosres.2012.10.011>.
- , S. Ringerud, L. Brucker, Y. You, I. de Gelis, and C. Prigent, 2020: An active-passive microwave land surface database from GPM. *IEEE Trans. Geosci. Remote Sens.*, **58**, 6224–6242, <https://doi.org/10.1109/TGRS.2020.2975477>.

- NASA, 2017: GPROF2017 version 1 and version 2 (used in GPM V5 processing). Algorithm Theoretical Basis Doc., 64 pp., http://rain.atmos.colostate.edu/ATBD/ATBD_GPM_October1_2017.pdf.
- Norouzi, H., M. Temimi, C. Prigent, F. J. Turk, R. Khanbilvardi, Y. Tian, F. A. Furuzawa, and H. Masunaga, 2015: Assessment of the consistency among global microwave land surface emissivity products. *Atmos. Meas. Tech.*, **8**, 1197–1205, <https://doi.org/10.5194/amt-8-1197-2015>.
- Panegrossi, G., J. F. Rysman, D. Casella, A. C. Marra, P. Sanò, and M. S. Kulie, 2017: CloudSat-based assessment of GPM Microwave Imager snowfall observation capabilities. *Remote Sens.*, **9**, 1263, <https://doi.org/10.3390/rs9121263>.
- Petković, V., C. D. Kummerow, D. L. Randel, J. R. Pierce, and J. K. Kodros, 2017: Improving the quality of heavy precipitation estimates from satellite passive microwave rainfall retrievals. *J. Hydrometeorol.*, **19**, 69–85, <https://doi.org/10.1175/JHM-D-17-0069.1>.
- , M. Orescanin, P.-E. Kirstetter, C. Kummerow, and R. R. Ferraro, 2019: Enhancing PMW satellite precipitation estimation: Detecting convective class. *J. Atmos. Oceanic Technol.*, **36**, 2349–2363, <https://doi.org/10.1175/JTECH-D-19-0008.1>.
- Petty, G. W., 2013: Dimensionality reduction in Bayesian estimation algorithms. *Atmos. Meas. Tech.*, **6**, 2267–2276, <https://doi.org/10.5194/amt-6-2267-2013>.
- , and R. Bennartz, 2017: Field-of-view characteristics and resolution matching for the Global Precipitation Measurement (GPM) Microwave Imager (GMI). *Atmos. Meas. Tech.*, **10**, 745–758, <https://doi.org/10.5194/amt-10-745-2017>.
- Prigent, C., F. Aires, and W. B. Rossow, 2003: Retrieval of surface and atmospheric geophysical variables over snow-covered land from combined microwave and infrared satellite observations. *J. Appl. Meteor.*, **42**, 368–380, [https://doi.org/10.1175/1520-0450\(2003\)042<0368:ROSAAG>2.0.CO;2](https://doi.org/10.1175/1520-0450(2003)042<0368:ROSAAG>2.0.CO;2).
- , —, and W. Rossow, 2006: Land surface microwave emissivities over the globe for a decade. *Bull. Amer. Meteor. Soc.*, **87**, 1573–1584, <https://doi.org/10.1175/BAMS-87-11-1573>.
- , E. Jaumouille, F. Chevallier, and F. Aires, 2008: A parameterization of the microwave land surface emissivity between 19 and 100 GHz, anchored to satellite-derived estimates. *IEEE Trans. Geosci. Remote Sens.*, **46**, 344–352, <https://doi.org/10.1109/TGRS.2007.908881>.
- , P. Liang, Y. Tian, F. Aires, J.-L. Moncet, and S. A. Boukabara, 2015: Evaluation of modeled microwave land surface emissivities with satellite-based estimates. *J. Geophys. Res. Atmos.*, **120**, 2706–2718, <https://doi.org/10.1002/2014JD021817>.
- Ringerud, S., C. D. Kummerow, and C. D. Peters-Lidard, 2014: A semi-empirical model for computing land surface emissivity in the microwave region. *IEEE Trans. Geosci. Remote Sens.*, **53**, 1935–1946, <https://doi.org/10.1109/TGRS.2014.2351232>.
- , —, and —, 2015: A prototype physical database for passive microwave retrievals of precipitation over the US Southern Great Plains. *J. Geophys. Res.*, **120**, 10 465–10 482, <https://doi.org/10.1002/2015JD023430>.
- , M. S. Kulie, D. L. Randel, G. M. Skofronick-Jackson, and C. D. Kummerow, 2019: Effects of ice particle representation on passive microwave precipitation retrieval in a Bayesian scheme. *IEEE Trans. Geosci. Remote Sens.*, **57**, 3619–3632, <https://doi.org/10.1109/TGRS.2018.2886063>.
- , C. Peters-Lidard, J. Munchak, and Y. You, 2020: Applications of dynamic land surface information for passive microwave precipitation retrieval. *J. Atmos. Oceanic Technol.*, **38**, 167–180, <https://doi.org/10.1175/JTECH-D-20-0048.1>.
- Romanov, P., G. Gutman, and I. Csiszar, 2000: Automated monitoring of snow cover over North America with multispectral satellite data. *J. Appl. Meteor.*, **39**, 1866–1880, [https://doi.org/10.1175/1520-0450\(2000\)039<1866:AMOSCO>2.0.CO;2](https://doi.org/10.1175/1520-0450(2000)039<1866:AMOSCO>2.0.CO;2).
- Rysman, J. F., G. Panegrossi, P. Sanò, A. C. Marra, S. Dietrich, L. Milani, and M. S. Kulie, 2018: SLALOM: An all-surface snow water path retrieval algorithm for the GPM Microwave Imager. *Remote Sens.*, **10**, 1278, <https://doi.org/10.3390/rs10081278>.
- , and Coauthors, 2019: Retrieving surface snowfall with the GPM Microwave Imager: A new module for the SLALOM algorithm. *Geophys. Res. Lett.*, **46**, 13 593–13 601, <https://doi.org/10.1029/2019GL084576>.
- Sanò, P., G. Panegrossi, D. Casella, F. Di Paola, L. Milani, A. Mugnai, M. Petracca, and S. Dietrich, 2015: The Passive microwave Neural network Precipitation Retrieval (PNPR) algorithm for AMSU/MHS observations: Description and application to European case studies. *Atmos. Meas. Tech.*, **8**, 837–857, <https://doi.org/10.5194/amt-8-837-2015>.
- Seto, S., N. Takahashi, and T. Iguchi, 2005: Rain/no-rain classification methods for microwave radiometer observations over land using statistical information for brightness temperatures under no-rain conditions. *J. Appl. Meteor.*, **44**, 1243–1259, <https://doi.org/10.1175/JAM2263.1>.
- , T. Iguchi, and T. Oki, 2013: The basic performance of a precipitation retrieval algorithm for the global precipitation measurement mission's single/dual-frequency radar measurements. *IEEE Trans. Geosci. Remote Sens.*, **51**, 5239–5251, <https://doi.org/10.1109/TGRS.2012.2231686>.
- Skofronick-Jackson, G., and B. T. Johnson, 2011: Surface and atmospheric contributions to passive microwave brightness temperatures for falling snow events. *J. Geophys. Res.*, **116**, D02213, <https://doi.org/10.1029/2010JD014438>.
- , —, and J. Munchak, 2013: Detection thresholds of falling snow from satellite-borne active and passive sensors. *IEEE Trans. Geosci. Remote Sens.*, **51**, 4177–4189, <https://doi.org/10.1109/TGRS.2012.2227763>.
- , D. Kirschbaum, W. Petersen, G. J. Huffman, C. Kidd, E. Stocker, and R. Kakar, 2018: The Global Precipitation Measurement (GPM) mission's scientific achievements and societal contributions: Reviewing four years of advanced rain and snow observations. *Quart. J. Roy. Meteor. Soc.*, **144**, 27–48, <https://doi.org/10.1002/qj.3313>.
- , M. Kulie, L. Milani, S. M. Munchak, N. B. Wood, and V. Levizzani, 2019: Satellite estimation of falling snow: A Global Precipitation Measurement (GPM) Core Observatory perspective. *J. Appl. Meteor. Climatol.*, **58**, 1429–1448, <https://doi.org/10.1175/JAMC-D-18-0124.1>.
- Smith, E. A., and Coauthors, 2013: Transitioning from CRD to CDRD in Bayesian retrieval of rainfall from satellite passive microwave measurements. Part 3: Identification of optimal meteorological tags. *Nat. Hazards Earth Syst. Sci.*, **13**, 1185–1208, <https://doi.org/10.5194/nhess-13-1185-2013>.
- Sun, Q., C. Miao, Q. Duan, H. Ashouri, S. Sorooshian, and K. Hsu, 2017: A review of global precipitation data sets: Data sources, estimation, and intercomparisons. *Rev. Geophys.*, **56**, 79–107, <https://doi.org/10.1002/2017RG000574>.
- Takbiri, Z., A. Ebtehaj, E. Foufoula-Georgiou, P. E. Kirstetter, and J. Turk, 2019: A prognostic retrieval approach for microwave precipitation phase detection over snow cover. *J. Hydrometeorol.*, **20**, 251–274, <https://doi.org/10.1175/JHM-D-18-0021.1>.
- Tan, J., G. J. Huffman, D. T. Bolvin, and E. J. Nelkin, 2019: IMERG V06: Changes to the morphing algorithm. *J. Atmos.*

- Oceanic Technol.*, **36**, 2471–2482, <https://doi.org/10.1175/JTECH-D-19-0114.1>.
- Tang, G., D. Long, A. Behrangi, C. Wang, and Y. Hong, 2018: Exploring deep neural networks to retrieve rain and snow in high latitudes using multisensor and reanalysis data. *Water Resour. Res.*, **54**, 8253–8278, <https://doi.org/10.1029/2018WR023830>.
- Tapiador, F. J., C. Kidd, K. L. Hsu, and F. S. Marzano, 2004: Neural networks in satellite rainfall estimation. *Meteor. Appl.*, **11**, 83–91, <https://doi.org/10.1017/S1350482704001173>.
- , and Coauthors, 2012: Global precipitation measurement: Methods, datasets and applications. *Atmos. Res.*, **104–105**, 70–97, <https://doi.org/10.1016/j.atmosres.2011.10.021>.
- , R. Roca, A. Del Genio, B. Dewitt, W. A. Petersen, and F. Zhang, 2019: Is precipitation a good metric for model performance? *Bull. Amer. Meteor. Soc.*, **100**, 223–233, <https://doi.org/10.1175/BAMS-D-17-0218.1>.
- Tassa, A., S. D. Michele, A. Mugnai, F. S. Marzano, and J. P. V. P. Baptista, 2003: Cloud model-based Bayesian technique for precipitation profile retrieval from the Tropical Rainfall Measuring Mission Microwave Imager. *Radio Sci.*, **38**, 8074, <https://doi.org/10.1029/2002RS002674>.
- Tian, Y., C. D. Peters-Lidard, K. W. Harrison, Y. You, S. Ringerud, S. Kumar, and F. J. Turk, 2015: An examination of methods for estimating land surface microwave emissivity. *J. Geophys. Res. Atmos.*, **120**, 11 114–11 128, <https://doi.org/10.1002/2015JD023582>.
- Turk, F. J., L. Li, and Z. S. Haddad, 2014a: A physically based soil moisture and Microwave Emissivity Data Set for Global Precipitation Measurement (GPM) applications. *IEEE Trans. Geosci. Remote Sens.*, **52**, 7637–7650, <https://doi.org/10.1109/TGRS.2014.2315809>.
- , Z. S. Haddad, and Y. You, 2014b: Principal components of multifrequency microwave land surface emissivities. Part I: Estimation under clear and precipitating conditions. *J. Hydrometeorol.*, **15**, 3–19, <https://doi.org/10.1175/JHM-D-13-08.1>.
- , R. Sikhakolli, P. Kirstetter, and S. L. Durden, 2015: Exploiting over-land *OceanSat-2* scatterometer observations to capture short-period time-integrated precipitation. *J. Hydrometeorol.*, **16**, 2519–2535, <https://doi.org/10.1175/JHM-D-15-0046.1>.
- , Z. S. Haddad, P. E. Kirstetter, Y. You, and S. Ringerud, 2017: An observationally based method for stratifying *a priori* passive microwave observations in a Bayesian-based precipitation retrieval framework. *Quart. J. Roy. Meteor. Soc.*, **144**, 145–164, <https://doi.org/10.1002/qj.3203>.
- Utsumi, N., F. J. Turk, Z. S. Haddad, P.-E. Kirstetter, and H. Kim, 2020: Evaluation of precipitation vertical profiles estimated by GPM-era satellite-based passive microwave retrievals. *J. Hydrometeorol.*, **22**, 95–112, <https://doi.org/10.1175/JHM-D-20-0160.1>.
- Wan, W., and Coauthors, 2019: Using CYGNSS data to monitor China's flood inundation during typhoon and extreme precipitation events in 2017. *Remote Sens.*, **11**, 854, <https://doi.org/10.3390/rs11070854>.
- Wang, D., and Coauthors, 2017: Surface emissivity at microwaves to millimeter waves over polar regions: Parameterization and evaluation with aircraft experiments. *J. Atmos. Oceanic Technol.*, **34**, 1039–1059, <https://doi.org/10.1175/JTECH-D-16-0188.1>.
- Wang, N.-Y., C. Liu, R. Ferraro, D. Wolff, E. Zipser, and C. D. Kummerow, 2009: TRMM2A12 land precipitation product-status and future plans. *J. Meteor. Soc. Japan*, **87**, 237–253, <https://doi.org/10.2151/jmsj.87A.237>.
- Wood, N. B., and T. L'Ecuyer, 2013: Level 2C snow profile process description and interface control document. JPL Doc., 21 pp., accessed 24 November 2020, http://www.cloudsat.cira.colostate.edu/sites/default/files/products/files/2C-SNOW-PROFILE_PDICD.P_R04.20130210.pdf.
- Yamamoto, M. K., S. Shige, C. K. Yu, and L. W. Cheng, 2017: Further improvement of the heavy orographic rainfall retrievals in the GSMaP algorithm for microwave radiometers. *J. Appl. Meteor. Climatol.*, **56**, 2607–2619, <https://doi.org/10.1175/JAMC-D-16-0332.1>.
- Yan, B., F. Weng, and H. Meng, 2008: Retrieval of snow surface microwave emissivity from the advanced microwave sounding unit. *J. Geophys. Res.*, **113**, D19206, <https://doi.org/10.1029/2007JD009559>.
- You, Y., F. J. Turk, Z. S. Haddad, L. Li, and G. Liu, 2014: Principal components of multifrequency microwave land surface emissivities. Part II: Effects of previous-time precipitation. *J. Hydrometeorol.*, **15**, 20–37, <https://doi.org/10.1175/JHM-D-13-07.1>.
- , C. Peters-Lidard, J. Turk, S. Ringerud, and S. Yang, 2017a: Improving overland precipitation retrieval with brightness temperature temporal variation. *J. Hydrometeorol.*, **18**, 2355–2383, <https://doi.org/10.1175/JHM-D-17-0050.1>.
- , N.-Y. Wang, R. Ferraro, and S. Rudlosky, 2017b: Quantifying the snowfall detection performance of the GPM microwave imager channels over land. *J. Hydrometeorol.*, **18**, 729–751, <https://doi.org/10.1175/JHM-D-16-0190.1>.
- , C. Peters-Lidard, N.-Y. Wang, J. Turk, S. Ringerud, S. Yang, and R. Ferraro, 2018: The instantaneous retrieval of precipitation over land by temporal variation at 19 GHz. *J. Geophys. Res. Atmos.*, **123**, 9279–9295, <https://doi.org/10.1029/2017JD027596>.